Unclassified

SECURITY CLASSIFICATION OF THIS PAGE (When Data Entered)

REPORT DOCUMENTATION PAGE

READ INSTRUCTIONS BEFORE COMPLETING FORM

1. REPORT NUMBER: IIHR Report No. 288

2. GOVT ACCESSION NO.:

3. RECIPIENT'S CATALOG NUMBER:

4. TITLE (and Subtitle): Effects of Waves on the Boundary Layer of a Surface-Piercing Body

5. TYPE OF REPORT & PERIOD COVERED: Technical Report November 1983 - May 1985

6. PERFORMING ORG. REPORT NUMBER: IIHR Report No. 288

7. AUTHOR(s): Frederick Stern

8. CONTRACT OR GRANT NUMBER(s): N00014-83-K-0136

9. PERFORMING ORGANIZATION NAME AND ADDRESS:
Iowa Institute of Hydraulic Research
The University of Iowa
Iowa City, Iowa 52242

10. PROGRAM ELEMENT, PROJECT, TASK AREA & WORK UNIT NUMBERS: NR 655-002

11. CONTROLLING OFFICE NAME AND ADDRESS:
Office of Naval Research
800 North Quincy Street
Arlington, Virginia 22217

12. REPORT DATE: May 1985

13. NUMBER OF PAGES:

14. MONITORING AGENCY NAME & ADDRESS (if different from Controlling Office):
Office of Naval Research
536 South Clark Street
Chicago, Illinois 60605

15. SECURITY CLASS. (of this report): Unclassified

15a. DECLASSIFICATION/DOWNGRADING SCHEDULE:

16. DISTRIBUTION STATEMENT (of this Report):

17. DISTRIBUTION STATEMENT (of the abstract entered in Block 20, if different from Report):

18. SUPPLEMENTARY NOTES:

19. KEY WORDS (Continue on reverse side if necessary and identify by block number):
Wave/Boundary Layer Interaction, 3-D Boundary Layer, Free Surface, Ship Boundary Layer

20. ABSTRACT (Continue on reverse side if necessary and identify by block number):

This report describes the results from an analytical and numerical study concerning the effects of waves on the boundary layer of a surface-piercing body. The boundary-value problem associated with the boundary-layer development on a surface-piercing body is formulated in a more rigorous manner in which proper consideration is given both to the kinematic and dynamic boundary conditions and to the deformation of the potential-flow free surface within the boundary layer. Simplifications that are appropriate for small amplitude

DD FORM 1 JAN 73 1473 EDITION OF 1 NOV 65 IS OBSOLETE
S/N 0102-LF-014-6601

Unclassified

SECURITY CLASSIFICATION OF THIS PAGE (When Data Enter

EFFECTS OF WAVES ON THE BOUNDARY LAYER OF A SURFACE-PIERCING BODY

by

Frederick Stern

Sponsored by

Office of Naval Research
Special Focus Research Program in Ship Hydrodynamics
Contract No. N00014-83-K-0136

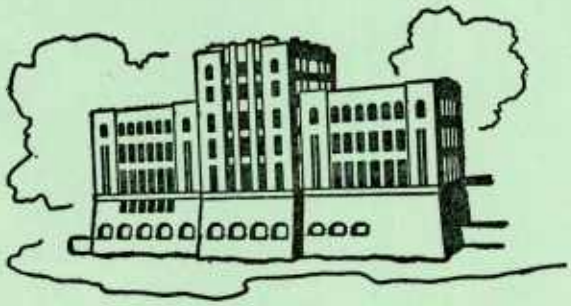

IIHR Report No. 288

~~Iowa~~ Institute of Hydraulic Research, University of Iowa,
The University of Iowa
Iowa City, Iowa 52242

May 1985

EFFECTS OF WAVES ON THE BOUNDARY LAYER OF A SURFACE-PIERCING BODY

by

Frederick Stern

Sponsored by

Office of Naval Research
Special Focus Research Program in Ship Hydrodynamics
Contract No. N00014-83-K-0136

IIHR Report No. 288

Iowa Institute of Hydraulic Research
The University of Iowa
Iowa City, Iowa 52242

May 1985

waves are then investigated. To this end, the flow field in the neighborhood of the body-boundary-layer/free-surface juncture is divided into five regions and order-of-magnitude estimates for each region are provided. Of particular interest is the body/free-surface boundary layer in the region very close to the free surface in which the free-surface boundary conditions have a significant influence. In this region, it is shown that, for laminar flow, the parameter Ak/ϵ , where Ak is the wave-steepness parameter and $\epsilon = \delta/L$ is the nondimensional boundary-layer thickness, is an important parameter for characterizing the flow. Different solution regimes are identified depending on the magnitude of Ak/ϵ . In particular, for Ak/ϵ sufficiently large such that the free-surface boundary conditions have a significant influence a consistent formulation requires the solution of the partially-parabolic Navier-Stokes equations. For turbulent flow, these conclusions cannot be reached with the same degree of certainty due to the present uncertainties in turbulence modelling, especially when a free surface is present. Numerical results are provided for the idealized geometry of a combination Stokes-wave/flat-plate. For this initial investigation, the usual thin-boundary-layer equations were solved using an existing three-dimensional finite-difference boundary-layer computer program that was modified to perform the present calculations. The primary purpose of the calculations is to demonstrate the influence of waves on boundary-layer development, including the effects of the free-surface boundary conditions, and to explore the limitations of the thin-boundary-layer equations prior to embarking on a more complete solution. For laminar flow, calculations were made using both an approximate and the small-amplitude-wave free-surface boundary conditions. The approximate boundary condition used is a symmetry (i.e. zero-gradient) condition which corresponds to a small-cross-flow solution along the mean free surface and a fully three-dimensional solution below. The influence of the free-surface boundary conditions is shown to be significant. For turbulent flow, calculations were made using the symmetry boundary condition only. Lastly, the implications of the present investigation for calculating ship boundary layers for nonzero Froude numbers are discussed.

Abstract

This report describes the results from an analytical and numerical study concerning the effects of waves on the boundary layer of a surface-piercing body. The boundary-value problem associated with the boundary-layer development on a surface-piercing body is formulated in a more rigorous manner in which proper consideration is given both to the kinematic and dynamic boundary conditions and to the deformation of the potential-flow free surface within the boundary layer. Simplications that are appropriate for small amplitude waves are then investigated. To this end, the flow field in the neighborhood of the body-boundary-layer/free-surface juncture is divided into five regions and order-of-magnitude estimates for each region are provided. Of particular interest is the body/free-surface boundary layer in the region very close to the free surface in which the free-surface boundary conditions have a significant influence. In this region, it is shown that, for laminar flow, the parameter Ak/ε, where Ak is the wave-steepness parameter and $\varepsilon = \delta/L$ is the nondimensional boundary-layer thickness, is an important parameter for characterizing the flow. Different solution regimes are identified depending on the magnitude of Ak/ε. In particular, for Ak/ε sufficiently large such that the free-surface boundary conditions have a significant influence a consistent formulation requires the solution of the partially-parabolic Navier-Stokes equations. For turbulent flow, these conclusions cannot be reached with the same degree of certainty due to the present uncertainties in turbulence modeling, especially when a free surface is present. Numerical results are provided for the idealized geometry of a combination Stokes-wave/flat-plate. For this initial investigation, the usual thin-boundary-layer equations were solved using an existing three-dimensional finite-difference boundary-layer computer program that was modified to perform the present calculations. The primary purpose of the calculations is to demonstrate the influence of waves on boundary-layer development, including the effects of the free-surface boundary conditions, and to explore the limitations of the thin-boundary-layer equations prior to embarking on a more complete solution. For laminar flow, calculations were made using both an approximate and the small-amplitude-wave free-surface boundary conditions. The approximate boundary condition used is a symmetry (i.e. zero-gradient) condition which corresponds to a small-cross-flow solution along the mean free surface and a fully three-dimensional solution below. The influence of the free-surface boundary conditions is shown to be signficant. For turbulent flow, calculations were made using the symmetry boundary condition only. Lastly, the implications of the present investigation for calculating ship boundary layers for nonzero Froude numbers are discussed.

Acknowledgement

I would like to acknowledge and thank Professors Landweber and Patel for their significant contributions to this work. Not only did they suggest the present topic to the author, but they also provided many helpful discussions. This research was sponsored by the Office of Naval Research, Special Focus Research Program in Ship Hydrodynamics, under Contract N00014-83-K-0136. The Graduate College of the University of Iowa provided a large share of the computer funds.

LIST OF SYMBOLS

Alphabetical Symbols

A	wave amplitude
A_j, B_j, C_j	coefficient matrices in the finite-difference equations (VI-9)-(VI-12)
Ak	wave steepness
a, b, c, h, g, f	components of the rate-of-strain tensor (IV-15)
c_p	pressure coefficient
$(\hat{e}_1, \hat{e}_2, \hat{e}_3)$	unit vectors in (x,y,z) direction
$(\hat{e}_n, \hat{e}_s, \hat{e}_t)$	unit vectors in normal and tangent directions to free surface
F	two- or three-dimensional vector of the principal dependent variables
h_i	metric coefficients in (x,y,z) directions
K_{ij}	the ij^{th} component of curvature
k	wave number
L	length of body (plate)
$\underline{n}$	normal vector the to free surface
P	fluid piezometric pressure
p	fluid pressure
p_o	ambient pressure
P_γ	surface-tension pressure
Q_e	edge velocity magnitude

$\overline{q^2}$	turbulent kinetic energy
R_n	Reynolds number
U,V,W	velocity components in the (x,y,z) directions
U_e, W_e	potential-flow edge velocities in the (x,z) directions
U_o	body speed
$\overline{u_i u_j}$	Reynolds stress tensor
$\underline{V}$	fluid velocity vector
$\underline{V}_e$	edge velocity vector
x,y,z	curvilinear coordinate system
x_o, y_o, z_o	Cartesian coordinate system

Greek Symbols

β	wall-shear-stress angle
γ	coefficient of surface tension
δ	boundary-layer thickness
δ^*	displacement thickness
δ_{ij}	Kronecker delta
ε	nondimensional boundary-layer thickness
ε_{ij}	rate-of-strain tensor (IV-14)
λ	wave length
μ	viscosity
ν	kinematic viscosity
ν_t	turbulent eddy-viscosity

η	free-surface displacement within the boundary layer
ρ	density
τ_w	wall-shear-stress magnitude
τ_{ij}	fluid stress tensor (IV-13)
τ^*_{ij}	external stress tensor
ϕ	wave velocity potential
∇	gradient

Subscripts

m	node-point index in y-direction
MM	maximum number of node-points in y-direction
n	node-point index in z-direction
NN	maximum number of node-points in z-direction
e	edge value, edge of boundary layer

Superscripts

ℓ	node-point index in x-direction

Table of Contents

EFFECTS OF WAVES ON THE BOUNDARY LAYER OF A SURFACE-PIERCING BODY

I. BACKGROUND

The boundary-layer development upon a body that intersects a free-surface can be greatly influenced by the presence of free-surface gravity waves. In particular, waves of sufficient steepness induce a region of flow separation near the free-surface, which is otherwise absent. The occurrence of separation significantly modifies both the viscous and the wave-resistance components, making this a problem of considerable engineering importance. In spite of this, very little detailed experimental or rigorous theoretical work has been done on this problem.

Most of the experimental data concerning the influence of free-surface waves on body boundary-layer development are for ship and offshore-structure resistance. Wu and Landweber (1963) and others have shown that, for ship models, the viscous resistance depends on the Froude number. Present methods for predicting forces on offshore structures (for example, Salvesen et al. 1982) require drag-coefficient data for surface-piercing circular cylinders oscillating in ambient wave fields. A compilation of such data (Sarpkaya and Isaacson 1981) shows large effects due to the presence of a wavy free-surface and wave-induced separation.

Surface shear-stress and pressure-distribution measurements have been made in towing tanks for various ship forms by Steele (1967), Steele and Pearce (1968), Tzou (1968) and Huang and von Kerczek (1972). The results from these experiments show considerable influence of Froude number on the shear stress and pressure distributions along waterlines close to the free-surface. More recent towing-tank experiments (again for various ship forms) have included some mean-velocity-profile measurements within the boundary layer (Doi 1980, Nagamatsu 1981, ITTC 1984). Most of the data are limited to the stern and near-wake region. Also, the Froude-number range is limited. Again, the results indicate effects due to the presence of the free surface and a dependence on Froude number. Very recently, mean-velocity and turbulence measurements were made in the stern and near-wake region of a double-tanker

model, in a circulating water channel, by Hotta and Hatano (1983). The data were obtained for one value of Froude number. The measurements indicate a local damping of the normal component of turbulence near the free-surface. This effect has also been observed in open-channel flows (Rodi 1980).

Only one investigation has been concerned specifically with wave-induced separation (Chow 1967). Chow demonstrated wave-induced separation experimentally with two-dimensional struts mounted vertically and piercing the free surface in a hydraulic flume. The struts were designed for unseparated flow when no waves are present, that is, at large depths. For an airfoil-like strut, Chow observed regions of separated flow originating just beyond the wave trough and extending to the strut trailing edge (see figure 1). The depth of the separated-flow region was on the order of the wave height. The length of the separated-flow region was shown to depend on Froude number. Chow also observed large secondary flow within the separated-flow region which he presumed was due to the curvature of the free-surface waves. He speculated that the flow separation was caused by the secondary flow.

Very few theoretical investigations of boundary-layer development on surface-piercing bodies have been performed. Furthermore, all of these investigations have been of an approximate nature and none have properly accounted for the free-surface kinematic and dynamic boundary conditions or the local damping of turbulence near the free surface. Most of the calculations that have been made utilize integral methods and assume small-cross-flow conditions (Lin and Hall 1966, Webster and Huang 1968, Gadd 1971, Adee 1972 and 1975, Sachdeva and Preston 1975, Doi 1980, Hinatsu and Takeshi 1985). Shahshahan and Patel (1983) calculated the boundary-layer along the body/wave intersection for Chow's model (see figure 1) and the Wigley hull using the small-cross-flow differential equations. These methods do indicate significant free-surface effects on boundary-layer development, including wave-induced separation at certain Froude numbers. Separation is judged to occur when the streamwise skin friction is zero or the cross-flow becomes large. In some cases, qualitative agreement with experimental data has been shown (Doi 1980 and Shahshahan and Patel 1983).

II. PHYSICAL PROBLEM

Consider the development of the boundary-layer upon a ship-like body, moving steadily at velocity U_o and intersecting the free-surface of an incompressible viscous fluid. This situation is depicted in figure 2. In distinction from the infinite fluid double-body problem, the present problem has special features due to the presence of the free surface and gravity waves (Patel et. al, 1983):

* the external-flow pressure field is influenced by the body wave-making such that it is Froude-number dependent;

* at the free surface, which is itself unknown and to be determined as part of the solution, there are two nonlinear boundary conditions, a kinematic one and a dynamic one, that the solution must satisfy;

* the characteristics of the structure of turbulence is modified near a free surface; and

* waves of sufficient steepness induce a region of flow separation near the free surface, which is otherwise absent.

In order to elucidate the effects of these special features on the body-boundary-layer development it is necessary to examine the flow in the neighborhood of the body-boundary-layer/free-surface juncture in somewhat more detail. As shown in figure 3, the flow field can be divided into five regions: I, potential-flow region in which viscous effects are negligible; II, free-surface boundary-layer region at a sufficient distance from the body that it is not influenced by the body boundary layer; III, body-boundary-layer region at a sufficient depth that it is not influenced by the free-surface boundary conditions; IV, body/free-surface boundary layer in the region very close to the free surface in which the free-surface boundary conditions have a significant influence; V, meniscus boundary-layer region.

In region III, the effects of the free surface are primarily transmitted through the external-flow pressure field and the flow-field order-of-magnitude estimates are well established. Over a large part of a ship-like body the thin-boundary-layer equations are applicable, and it is only in the stern region that it is necessary to solve the more complete partially-parabolic

Reynolds equations (Patel 1982). The order-of-magnitude estimates for regions I and II are also well established; however, this is not the case for regions IV and V.

In region IV, the effects of the free surface are due both to the influences of the external-flow pressure field and the kinematical and dynamical requirements of the free-surface boundary conditions. The kinematic boundary condition expresses the requirement that the free surface is a stream surface. The dynamic boundary condition expresses the requirement of continuity of the normal and tangential stresses across the free surface. The free-surface boundary conditions influence both the mean and the turbulent velocity components. The limited experimental data that are available indicate that, near a free surface, the normal component of turbulence is damped and the longitudinal and transverse components are increased. The turbulence structure near a solid wall shows similar characteristics, but there the situation is complicated by the influence of high strain rates due to the no-slip condition. The strain-rate magnitudes in regions IV and V are as yet not well established. Note that region IV is kinematically similar to the flow in a streamwise corner for which it is known that two length scales are important and the thin-boundary-layer equations are not applicable.

The precise physics in Region V is a complex matter involving surface tension. It is known that the shape of the meniscus depends upon the nature of the body surface finish and that it can have a very sharp angle of contact. According to Mei (1983), this subject appears to be a poorly understood part of physical chemistry.

III. SCOPE

The previous two discussions indicate both the complexity and present limited understanding of the effects of waves on the boundary layer of a surface-piercing body. In this report an effort is made to increase our understanding of the flow in regions III and IV (see figure 3).

First, the boundary-value problem associated with the boundary-layer development on a surface-piercing body is formulated in a more rigorous manner

in which proper consideration is given both to the kinematic and dynamic boundary conditions and to the deformation of the potential-flow free surface within the boundary layer. Simplifications that are appropriate for small-amplitude waves are then investigated. This is consistent with the usual approximation for calculating the outer wave potential in which linearized small-amplitude wave theory is used. Initially, in Sections IV and V the above analysis is performed for laminar flow so that definitive conclusions can be reached concerning the flow-field order-of-magnitude estimates for region IV. It is shown that the parameter Ak/ε, where Ak is the wave-steepness parameter and $\varepsilon = \delta/L$ is the nondimensional boundary-layer thickness, is an important parameter for characterizing the flow. Different solution regimes are identified depending on the magnitude of Ak/ε. In particular, for Ak/ε sufficiently large such that the free-surface boundary conditions have a significant influence, a consistent formulation requires the solutions of the partially-parabolic Navier-Stokes equations. Thus region IV is, in fact, analogous to the flow in a streamwise corner.

Next, in Section VI, laminar-flow numerical results are provided for the idealized geometry of a combination Stokes-wave/flat-plate. This geometry is considered optimum for the present investigation, since it is simple, yet the flow near the free-surface is fully three-dimensional. Far from the free-surface and for laminar flow, the solution is the well-known Blasius one. For this initial investigation, the usual thin-boundary-layer equations were solved using an existing three-dimensional finite-difference boundary-layer computer program that was modified to perform the present calculations. The primary purpose of the calculations is to demonstrate the influence of waves on boundary-layer development, including the effects of the free-surface boundary conditions, and to explore the limitations of the thin-boundary-layer equations prior to embarking on a more complete solution. Results are presented from calculations performed using both an approximate and the small-amplitude-wave free-surface boundary conditions.

In Section VII, the necessary extensions for turbulent-flow analysis are considered. In this case, it is not possible to determine the order-of-magnitude estimates for region IV with the same degree of certainty. This is due to the present uncertainties in turbulence modelling, especially when a

free surface is present. A brief discussion is included concerning this difficult topic. The influence of turbulence on the previous laminar-flow symmetry-condition results is then studied. For this purpose, a simple modification is made to a one-equation wall-turbulence model to account for the influence of the free surface.

Lastly, in Section VII, a summary of the results from the present investigation is provided, and in Section VIII, the implications of the present investigation and the necessary extensions that are required for calculating ship boundary layers for nonzero Froude numbers are discussed.

IV. LAMINAR-FLOW PROBLEM FORMULATION

For ease of explication and since the numerical results to be presented are for the thin-boundary-layer equations, the governing differential equations presented are the usual thin-boundary-layer equations which are written in orthogonal curvilinear coordinates (Nash and Patel 1972)

$$\frac{U}{h_1}\frac{\partial U}{\partial x} + \frac{V}{h_2}\frac{\partial U}{\partial y} + \frac{W}{h_3}\frac{\partial U}{\partial z} + (K_{13}U - K_{31}W)\,W + \frac{1}{h_1}\frac{\partial}{\partial x}(P/\rho) - \frac{\nu}{h_2}\frac{\partial}{\partial y}\left(\frac{1}{h_2}\frac{\partial U}{\partial y}\right) = 0 \qquad \text{(IV-1)}$$

$$\frac{1}{h_2}\frac{\partial}{\partial y}(P/\rho) = 0 \qquad \text{(IV-2)}$$

$$\frac{U}{h_1}\frac{\partial W}{\partial x} + \frac{V}{h_2}\frac{\partial W}{\partial y} + \frac{W}{h_3}\frac{\partial W}{\partial z} + (K_{31}W - K_{13}U)\,U + \frac{1}{h_3}\frac{\partial}{\partial z}(P/\rho) - \frac{\nu}{h_2}\frac{\partial}{\partial y}\left(\frac{1}{h_2}\frac{\partial W}{\partial y}\right) = 0 \qquad \text{(IV-3)}$$

$$\frac{1}{h_1}\frac{\partial U}{\partial x} + \frac{1}{h_2}\frac{\partial V}{\partial y} + \frac{1}{h_3}\frac{\partial W}{\partial z} + (K_{21} + K_{31})\,U + (K_{13} + K_{23})\,W = 0 \qquad \text{(IV-4)}$$

where $\underline{V}$ = (U, V, W) and P are the velocity components and piezometric pressure, ρ is the fluid density and ν is the fluid kinematic viscosity. The h_i are the metrical coefficients associated with the (x,y,z) coordinates and $K_{ij} = \frac{1}{h_i h_j} (\partial h_i / \partial x_j)$ is the curvature of the x_i coordinate curve with x_j = constant.[3] Consistent with thin-boundary-layer theory, the (x,y,z) coordinate system is constructed such that the parametric curves x = constant and z = constant form an orthogonal grid upon the body surface and the y-coordinate is normal to the body surface. Such a coordinate system is only truly orthogonal on the body surface itself; however, the deviation from orthogonality off the body surface is presumed of higher order. There are a number of methods for constructing such a coordinate system. The external flow is assumed to be known either from experiment or inviscid-flow theory. It should be recognized that determination of this in itself may be a formidable task for an arbitrary three-dimensional body.

In consideration of the above and for specified initial conditions and appropriate boundary conditions, the system of equations (IV-1) - (IV-4) can be solved for (U,V,W). It is assumed that the initial conditions are known. The appropriate boundary conditions for the present problem are now considered. Referring to figure 4, which shows the projection of a surface x = constant onto a transverse plane (x_0 = constant), we have the following boundary conditions:

1) on the surface of the body (y = 0);

$$U = V = W = 0 \tag{IV-5}$$

2) at the edge of the boundary layer ($y = \delta$);

$$U = U_e, \; W = W_e \tag{IV-6}$$

3) on the plane-of-symmetry;

$$W = 0, \; \frac{\partial U}{\partial z} = 0 \tag{IV-7}$$

4) on the free-surface ($z=\eta$) there are two boundary conditions;

$$\text{kinematic boundary condition: } \underline{V} \cdot \underline{n} = 0 \tag{IV-8}$$

$$\text{dynamic boundary condition: } \tau_{ij} n_j = \overset{*}{\tau}_{ij} n_j \tag{IV-9}$$

where $\underline{n} = (n_1, n_2, n_3)$ is the outward normal vector to the free surface and τ_{ij} and $\overset{*}{\tau}_{ij}$ are the fluid and external stress tensors, respectively. Within the boundary layer, the free surface is deformed and does not coincide with the potential-flow free surface; consequently, within the boundary layer, just as is the case in the outer flow, the free surface must be determined as part of the solution. In general, the free surface within the boundary layer can be expressed by an equation of the form (see figure 5)

$$z = \eta(x,y) \tag{IV-10}$$

thus

$$\underline{n} = - \eta_x \hat{e}_1 - \eta_y \hat{e}_2 + \hat{e}_3$$

where

$$\eta_x = \frac{1}{h_1} \frac{\partial \eta}{\partial x}, \quad \eta_y = \frac{1}{h_1} \frac{\partial \eta}{\partial y}$$

and $(\hat{e}_1, \hat{e}_2, \hat{e}_3)$ are the unit vectors in the (x,y,z) directions.

The kinematic free-surface boundary condition (IV-8) expresses the requirement that the free-surface be a stream surface. The dynamic boundary condition (IV-9) expresses the requirement of continuity of the normal and tangential stresses across the free surface (see figure 6). The external stress is simply given by the difference between the ambient pressure p_o and the surface-tension pressure

$$p_\gamma = \gamma \hat{e}_n \cdot \left[\frac{\partial \hat{e}_s}{\partial s} + \frac{\partial \hat{e}_t}{\partial t}\right] \tag{IV-11}$$

thus

$$\overset{*}{\tau}_{ij} = - (p_o - p_\gamma)\, \delta_{ij} \tag{IV-12}$$

where γ is the coefficient of surface tension, $\hat{e}_n$ is the unit normal vector, $(\hat{e}_s, \hat{e}_t)$ are two unit tangent vectors and δ_{ij} is the Kronecker-delta func-

tion. For Cartesian coordinates, p_γ is simply given by

$$p_\gamma = \frac{\gamma(\eta_{x_o x_o} + \eta_{y_o y_o})}{[1 + \eta_{x_o}^2 + \eta_{y_o}^2]^{3/2}}$$

Stokes' law provides the fluid stress

$$\tau_{ij} = -p\delta_{ij} + 2\mu\varepsilon_{ij} \qquad \text{(IV-13)}$$

where μ is the fluid viscosity, p is the fluid pressure and ε_{ij} is the rate-of-strain tensor

$$\varepsilon_{ij} = \begin{bmatrix} a & h/2 & g/2 \\ h/2 & b & f/2 \\ g/2 & f/2 & c \end{bmatrix} \qquad \text{(IV-14)}$$

with

$$\begin{aligned} a &= \frac{1}{h_1}\frac{\partial U}{\partial x} + VK_{12} + WK_{13} \\ b &= \frac{1}{h_2}\frac{\partial V}{\partial y} + WK_{23} + UK_{21} \\ c &= \frac{1}{h_3}\frac{\partial W}{\partial z} + UK_{31} + VK_{32} \\ f &= \frac{1}{h_3}\frac{\partial V}{\partial z} - VK_{23} + \frac{1}{h_2}\frac{\partial W}{\partial y} - WK_{32} \\ g &= \frac{1}{h_1}\frac{\partial W}{\partial x} - WK_{31} + \frac{1}{h_3}\frac{\partial U}{\partial z} - UK_{13} \\ h &= \frac{1}{h_2}\frac{\partial U}{\partial y} - UK_{12} + \frac{1}{h_1}\frac{\partial V}{\partial x} - VK_{21} \end{aligned} \qquad \text{(IV-15)}$$

By means of the previous definitions, the free-surface boundary conditions (IV-8) and (IV-9) can be expressed by

$$-\eta_x U - \eta_y V + W = 0 \qquad \text{(IV-16)}$$

$$p\eta_x + \mu[-2a\eta_x - h\eta_y + g] = (p_o - p_\gamma)\,\eta_x \qquad \text{(IV-17)}$$

$$p\eta_y + \mu\,[-h\eta_x - 2b\eta_y + f] = (p_o - p_\gamma)\,\eta_y \qquad \text{(IV-18)}$$

$$-p + \mu[-g\eta_x - f\eta_y + 2c] = -(p_o - p_\gamma) \qquad \text{(IV-19)}$$

Conditions (IV-16) - (IV-19) are to be applied on the unknown surface $z = \eta(x,y)$. Note that conditions (IV-16) - (IV-19) are linear in the free-surface slopes (η_x, η_y), and thus two of the conditions can be used to eliminate (η_x, η_y) by expressing them in terms of the pressure difference $(p - p_o + p_\gamma)$, the fluid velocity components and the rates-of-strain. The remaining two conditions, with (η_x, η_y) known, can then be used to provide boundary conditions in the solution of the momentum equations. No approximations have been made in deriving conditions (IV-16) - (IV-19) and, as such, the formulated boundary-value problem constitutes a fully nonlinear free-surface problem. Presumably, conditions (IV-16) - (IV-19) are sufficient, in conjunction with the remainder of the boundary-value problem, to render a unique solution, including the free-surface itself.

V. SMALL-AMPLITUDE-WAVE SOLUTION

Consideration is now given to appropriate simplifications of the free-surface boundary conditions that are consistent with small-amplitude waves. To this end, it is necessary to determine the order-of-magnitude estimates for region IV (see figure 3). This is accomplished by considering both the established order-of-magnitude estimates in the surrounding regions I-III and the requirements imposed by the free-surface boundary conditions. These estimates are then applied to the governing equations and different solution regimes are identified.

In Region I (potential flow), consistent with small-amplitude wave theory, the flow-field order-of-magnitude estimates are as follows:

$$\begin{aligned} &U = U_o + u \sim 0(1) && \varepsilon_{ij} \sim 0(Ak) \\ &(u,V,W) \sim 0(Ak) && \eta \sim 0(Ak) \\ & && \nabla\eta \sim 0(Ak) \end{aligned} \qquad \text{(V-1)}$$

where U_o is the body speed, A is the characteristic wave amplitude and k the characteristic wave number. The most important nondimensional parameter in this region is Ak, the wave steepness, and for small-amplitude wave theory to be valid, $Ak << 1$.

Region II is the part of the free-surface boundary layer above region I and is due to the condition of zero stress on the free-surface in a viscous fluid (for example, Kinsman 1965 or Mei 1983). For laminar flow, the thickness of this boundary layer is

$$\delta_{fs} = \frac{\sqrt{2}}{k} R_w^{-1/2} \qquad \text{(V-2)}$$

where $R_w = C/\nu k$ is the wave Reynolds number and $C = U_o$ is the wave celerity. δ_{fs} is of the same order of magnitude as the body boundary layer

$$\delta_b \propto R_b^{-1/2} \qquad \text{(V-3)}$$

where $R_b = \frac{U_o L}{\nu}$ is the body Reynolds number; since, for most circumstances, the wave length $\lambda = \frac{2\pi}{k} \simeq L$. However, the free-surface boundary layer is very weak and has a negligible influence ($0(\delta_{fs}^2)$) on the potential flow kinematics and dynamics. Evidently, the zero-stress condition places a much less severe restriction on the flow field than the wall-boundary-layer no-slip condition, resulting in only minor adjustments to the potential-flow velocity field. The flow-field order-of-magnitude estimates for region II are the same as for region I.

Region III, is the body-boundary-layer region sufficiently deep below the free surface that it is not influenced by the free-surface boundary conditions. Based on region II considerations, it is expected that the required depth is of $0(\delta_b)$. At this depth the effects of the free surface are primarily transmitted through the external-flow pressure field and the flow-field order-of-magnitude estimates are well established (Nash and Patel 1972):

$$\begin{aligned} (U,W) &\sim 0(1) & \left(\frac{\partial}{\partial x}, \frac{\partial}{\partial z}\right) &\sim 0(1) \\ V &\sim 0(\varepsilon) & \frac{\partial}{\partial y} &\sim 0(\varepsilon^{-1}) \end{aligned} \qquad \text{(V-4)}$$

where $\varepsilon = \delta_b/L$ is the most important nondimensional parameter for this region and, for thin-boundary-layer theory to be valid, $\varepsilon << 1$.

Region IV is the body/free-surface boundary-layer overlap region. Near the free surface, the region III order-of-magnitude estimates (V-4) will be modified due to wave effects. The wave effects are characterized by the parameter Ak. Thus there are two important nondimensional parameters for region IV, ε and Ak. In order for boundary-layer theory (thick or thin) to be valid, some of the above order-of-magnitude estimates (V-4) must be retained:

$$\begin{aligned} U &\sim O(1) & \frac{\partial}{\partial x} &\sim O(1) \\ V &\sim O(\varepsilon) & \frac{\partial}{\partial y} &\sim O(\varepsilon^{-1}) \end{aligned} \qquad \text{(V-5)}$$

For small-amplitude waves, it can be assumed that, within the boundary layer,

$$\begin{aligned} \eta &\sim O(Ak) \\ W &\sim O(Ak) \end{aligned} \qquad \text{(V-6)}$$

just as they are in the outer flow. This assumption implies that the magnitude of the coordinate cuvatures K_{13} and K_{31} in region IV are ≥ 0 (Ak). The order-of-magnitude of $\frac{\partial}{\partial z}$ is to be determined next. This is accomplished by using equation (IV-19) to eliminate the pressure difference $p - p_o + p_\gamma$ in equations (IV-17) and (IV-18) which yields

$$2(c-a)\eta_x - h\eta_y + g = g\eta_x^2 + f\eta_x\eta_y \qquad \text{(V-7)}$$

$$-h\eta_x + 2(c-b)\,\eta_y + f = g\eta_x\eta_y + f\eta_y^2$$

and taking orders-of-magnitude to obtain

$$U_z \gtrsim O\left(\frac{Ak}{\varepsilon^2}\right)$$

$$V_z \gtrsim O\left(\frac{Ak}{\varepsilon}\right) \qquad \text{(V-8)}$$

which imply that

$$\frac{\partial}{\partial z} \gtrsim O\left(\frac{Ak}{\varepsilon^2}\right) \qquad \text{(V-9)}$$

Here the equality in (V-9) can be assumed since this represents the most restrictive case. The region IV order-of-magnitude estimates are summarized in table 1. The above analysis indicates that the ratio Ak/ε is an important parameter in characterizing the flow in region IV. In fact, as will now be discussed, different solution regimes can be identified according to the magnitude of Ak/ε.

Table 1. Body/Free-Surface Boundary Layer Order-of-Magnitude Estimates

	order-of-magnitude
U	1
V	ε
W	Ak
$\partial/\partial x$	1
$\partial/\partial y$	ε^{-1}
$\partial/\partial z$	Ak/ε^2
η	Ak
η_x	Ak
η_y	Ak/ε
ν	ε^2

For this purpose, it is assumed that the order of magnitude of Ak is given by

$$Ak \sim 0(\varepsilon^{n}) \quad \text{(V-10)}$$

Using the results from table 1 along with (V-10) in the momentum equations (IV-1) and (IV-3) it can be seen that the z-derivative terms have the orders of magnitude

$$\frac{W}{h_3}\frac{\partial U}{\partial z} \sim 0(\varepsilon^{2n-2}) \quad \text{(V-11)}$$

$$\frac{W}{h_3}\frac{\partial W}{\partial z} \sim Ak0(\varepsilon^{2n-2}) \quad \text{(V-12)}$$

This shows that the z-derivative terms can be neglected for $n > 1.5$. Therefore, this regime is similar to the small-cross-flow approximation which has been used by some investigators. Note that in the limit as $n \to \infty$ $Ak = 0$; that is, the free surface is flat and the flow is locally simply two-dimensional. For $n < 1.5$, the z-derivative terms cannot be neglected since they are of comparable order of magnitude to the other terms in the equations. Also, consideration of the order of magnitude of the z-diffusion terms that are neglected in the thin-boundary-layer equations shows that they are of the same order of magnitude as the terms in (V-11) and (V-12) for the x- and z-momentum equations, respectively. Therefore, for consistency, these terms cannot be neglected either. Furthermore, many of the terms neglected in the y-momentum equation (IV-2) are also of comparable order of magnitude and cannot be neglected. In fact, for $n = 1$ the order of magnitude estimates in region IV become,

$$\begin{aligned} U &\sim 0(1) & \frac{\partial}{\partial x} &\sim 0(1) \\ (V,W) &\sim 0(\varepsilon) & \left(\frac{\partial}{\partial y}, \frac{\partial}{\partial z}\right) &\sim 0(\varepsilon^{-1}) \end{aligned} \quad \text{(V-13)}$$

which are identical to those used by Patel (1982) in deriving the partially-parabolic Reynolds equations. Thus, it is seen that region IV is analogous to the flow in a streamwise corner as was indicated in Section II.

The free-surface boundary conditions (IV-16) - (IV-19) are to be applied on the unknown surface $z = \eta(x,y)$. However, using the same technique as that used in the outer flow, conditions (IV-16) - (IV-19) can be expanded in a Taylor Series about the known surface $z = 0$ and evaluated up to the desired order of approximation. To the lowest order of approximation conditions (IV-16) - (IV-19) are retained and simply evaluated on $z = 0$. Such a technique is restricted in the present application to $0(Ak/\varepsilon) > 1$ based on the previous order-of-magnitude analysis, since for $0(Ak/\varepsilon) < 1$ the Taylor series expansions are not convergent. Consequently, for $0(Ak/\varepsilon) < 1$ a small-amplitude-wave solution is not valid and the free-surface boundary conditions must be applied on the actual free surface $z = \eta$.

For small-amplitude-waves ($0(Ak/\varepsilon) > 1$) and in consideration of the table 1 order-of-magnitude estimates the highest-order terms in the free-surface boundary conditions (IV-16) - (IV-19) are

$$-\eta_x U - \eta_y V + W = 0, \qquad 0(Ak) \qquad \text{(V-14)}$$

$$-h\eta_y + g = 0, \qquad 0\left(\frac{Ak}{\varepsilon^2}\right) \qquad \text{(V-15)}$$

$$-h\eta_x - 2b\eta_y + f = 0, \qquad 0\left(\frac{Ak}{\varepsilon}\right) \qquad \text{(V-16)}$$

on $z = 0$

$$-(p - p_o + p_\gamma) + \mu\,[-g\eta_x - f\eta_y + 2c] = 0, \qquad 0\left(\varepsilon^2 \left(\frac{Ak}{\varepsilon}\right)^2\right) \qquad \text{(V-17)}$$

where the order of magnitude of the terms in conditions (V-14) - (V-17) is shown to the right of each equation. In the present investigation both p_γ and $(p - p_o)$ have been neglected in (V-17). The former approximation is consistent with neglecting region V. The y-momentum equation (IV-2) implies that within the context of thin-boundary-layer theory

$$p - p_o = \rho g(\eta_e - \eta) \qquad \text{on } z=0$$

where g is the gravitational acceleration and η_e is the potential-flow free surface; however, this effect was neglected. With these approximations (V-17) becomes

$$- g \eta_x - f\eta_y + 2c = 0 \qquad 0((\frac{Ak}{\varepsilon})^2) \qquad \text{(V-18)}$$

VI. STOKES-WAVE/FLAT-PLATE BOUNDARY LAYER

Calculations have been performed that demonstrate the influence of free-surface waves on body-boundary-layer development using the idealized geometry of a combination Stokes-wave/flat-plate. This flow configuration is considered optimum for the present investigation, since it is simple, yet the flow near the free surface is fully three-dimensional and of the same character as that generated by the wave-making of a surface-piercing body. Far from the free surface and for laminar flow, the solution is the well-known Blasius one. For laminar flow, calculations were made using both an approximate and the small-amplitude-wave free-surface boundary conditions. The approximate boundary condition used is a symmetry (i.e. zero-gradient) condition which corresponds to a small-cross-flow solution along the mean free surface and a fully three-dimensional solution below. Of particular interest was the influence of wave steepness on the boundary-layer development.

Consider the flow field in the vicinity of a surface-piercing vertical flat plate moving in and at the same speed as a simple harmonic wave train. It is assumed that the plate is sufficiently thin that it generates no wave of its own. Such a flow can be simulated in a towing tank either by towing the plate at the same speed as a wave-maker generated harmonic wave train or by towing the plate and generating the wave system with a submerged horizontal foil afixed ahead of the plate leading edge.* Outside of the plate boundary layer, the flow is essentially inviscid (see figure 3) and can be represented

---

* An experiment using the latter arrangement is presently under way at The University of Iowa's Institute of Hydraulic Research, the results of which will be reported in the near future.

mathematically as a first-order Stokes wave; that is, the fluid velocity field $\underline{V}_e$ for coordinates moving with the plate/wave system is simply given by:

$$\underline{V}_e = U_o \hat{e}_1 + \nabla \phi \qquad \text{(VI-1)}$$

where ϕ is the velocity potential

$$\phi = - AU_o e^{-kz} \sin kx \qquad \text{(VI-2)}$$

and (x,z) are Cartesian coordinates with x positive downstream and z positive downwards (see figure 7).** The third coordinate y is normal to the plate and across the boundary layer. The potential-flow free-surface elevation $\eta(x)$ and piezometric pressure coefficient c_p are given by

$$\eta(x) = A \cos kx \qquad \text{(VI-3)}$$

$$c_p(x,z) = 2\, Ak\, e^{-kz} \cos kx \qquad \text{(VI-4)}$$

With regard to calculating the boundary layer on the plate, the most important quantities are the edge velocities

$$U_e/U_o = 1 - Ak\, e^{-kz} \cos kx \qquad \text{(VI-5)}$$

$$W_e/U_o = Ak\, e^{-kz} \sin kx \qquad \text{(VI-6)}$$

and the pressure gradients

$$\frac{\partial}{\partial x}\left(\frac{p}{\rho U_o^2}\right) = - Ak^2 e^{-kz} \sin kx \qquad \text{(VI-7)}$$

$$\frac{\partial}{\partial z}\left(\frac{p}{\rho U_o^2}\right) = - Ak^2 e^{-kz} \cos kx \qquad \text{(VI-8)}$$

** Note that for the present application there is no need to distinguish between Cartesian and curvilinear coordinates and thus the subscript o has been dropped (see figure 2).

The wave elevation, edge velocities and pressure gradients are shown in figure 7. Referring to figure 7, it is seen that four potential-flow regions can be distinguished. In region I, both p_z and p_x are favorable, $W_e > 0$ and accelerating and $U_e < U_o$ and accelerating. In region II, p_x is favorable and p_z is adverse, $W_e > 0$ and decelerating and $U_e > U_o$ and accelerating. In region III, both p_z and p_x are adverse, $W_e < 0$ and decelerating and $U_e > U_o$ and decelerating. In region IV, p_z is favorable and p_x is adverse, $W_e < 0$ and accelerating and $U_e < U_o$ and decelerating. Each of these regions has a distinct influence on the boundary-layer development as will be discussed subsequently.

A. Computational Method. The governing differential equations (IV-1) - (IV-4) must be integrated numerically to obtain the fluid velocity field (U, V, W). It was decided from the outset that, if possible, an existing finite-difference method of integrating the three-dimensional boundary-layer equations would be modified for performing the present calculations. However, the requirements on such a method for the present application eliminated many of the more commonly used methods. Specifically, the method to be used must allow for cross-flow reversal and be sufficiently flexible in the prescription of boundary conditions to permit the specification of the free-surface boundary conditions (V-14) - (V-17) as discussed previously. These requirements are only met by methods that are fully implicit. One such method is that of Nash and Scruggs (1976), originally developed for aircraft applications. Subsequently, this method was improved by Patel et al (1979, 1983 and 1985) and applied to bodies of revolution at incidence and to ship forms for zero Froude number. This method was used for the present calculations. A number of modifications were required, as will be discussed next in conjunction with a brief review of the overall procedure.

The boundary-layer equations (IV-1) and (IV-3) can be written in matrix vector form

$$A_1 F + A_2 \frac{\partial F}{\partial x} + A_3 \frac{\partial F}{\partial z} + A_4 \frac{\partial F}{\partial y} + A_5 \frac{\partial^2 F}{\partial y^2} + A_6 = 0 \qquad \text{(VI-9)}$$

where $F^T = (U,W)$ and the $A_1 - A_6$ are coefficient matrices. By approximating each of the derivatives in (VI-9) by finite differences, equation (VI-9) can

be expressed as

$$B_1 F^{\ell}_{m+1,n} + B_2 F^{\ell}_{m,n+1} + B_3 F^{\ell}_{m,n} + B_4 F^{\ell}_{m-1,n} + B_5 F^{\ell}_{m,n-1} = B_6 F^{\ell-1}_{m,n} - A_6 \quad \text{(VI-10)}$$

where (ℓ,m,n) are node-point indexes in the (x,y,z) directions respectively and the B_1 - B_6 are coefficient matrices composed of linear combinations of the A's divided by the appropriate spatial difference. In obtaining equation (VI-10) the x-derivative in (VI-9) is expressed as a backward difference, the first-order z- and y-derivatives are expressed using upwind differencing so as to preserve convective stability and lastly the second-order y-derivative is expressed using a central difference. Thus, the overall procedure is only first-order accurate. The finite-difference molecule associated with (VI-10) is shown in figure 8. Note that both equations (VI-9) and (VI-10) are nonlinear since the coefficient matrices are functions of F. Equation (VI-10) is solved by means of an alternating-direction-implicit (ADI) scheme.

The forward marching procedure advances in the positive x-direction from a cross-plane $\ell-1$, where the solution is assumed to be known, to a cross-plane ℓ, at which a new solution is obtained from the solution of equation (VI-10) (see figure 8). The ADI scheme consists of scanning the cross-plane alternately in the n- and m-directions, converting equation (VI-10) respectively into the successive forms

$$B_1 F^{\ell}_{m+1,n} + B_3 F^{\ell}_{m,n} + B_4 F^{\ell}_{m-1,n} = C_1 \quad \text{(VI-11)}$$

$$B_2 F^{\ell}_{m,n+1} + B_3 F^{\ell}_{m,n} + B_5 F^{\ell}_{m,n-1} = C_2 \quad \text{(VI-12)}$$

in which C_1 and C_2 contain the passive terms originating from the left-hand side of (VI-10). The coefficients of equations (VI-11) and (VI-12) form a block-tridiagonal matrix and which is solved by an extended Thomas algorithm. After each n- or m-scan, the continuity equation is integrated to obtain the V velocity component. The B and C matrices are updated in successive iterations until convergence is obtained with respect to the velocity components at each grid point within a specified tolerance.

The thickness of the integration domain is $1.26\,\delta(x,z)$. Note that δ is determined as part of the solution. The number of grid points is kept constant in both the y- and z-directions. For laminar flow, a uniform distribution of grid points is used across the boundary layer. An expanding grid was used in the z-direction so as to allow for a higher concentration of grid points near the free-surface. A diverging geometric series was used for this purpose. The step size Δx is arbitrarily specified. The number of cross-plane grid points and the step size Δx are determined from accuracy and computer-cost considerations.

The boundary conditions imposed when solving equation (VI-10) at each cross-plane are:

$$F = 0 \qquad \text{on } y = 0 \qquad \text{(IV-13)}$$

$$\frac{\partial F}{\partial y} = 0 \qquad \text{on } y = 1.26\delta \qquad \text{(VI-14)}$$

$$\frac{\partial F}{\partial z} = 0 \qquad \text{on } z = z_{max} \qquad \text{(VI-15)}$$

$$\frac{\partial F}{\partial z} = C_3 \qquad \text{on } z = 0 \qquad \text{(VI-16)}$$

Condition (VI-13) is the no-slip condition: $F^{\ell}_{o,n} = 0$. Condition (VI-14) imposes the condition that the viscous-flow solution merge smoothly with the outer potential flow and is implemented by

$$F^{\ell}_{MM-1,n} = F^{\ell}_{MM,n}$$

where MM is the maximum number of grid points across the boundary layer. The zero-gradient matching condition does not insure that the edge values of $F^{\ell}_{MM,n}$ are identically (U_e, W_e) and small differences can occur; thus, after a converged solution is obtained at each cross-plane the velocity profiles are scaled with the known values of (U_e, W_e). Condition (VI-15) is a symmetry condition and is implemented by

$$F^{\ell}_{m,NN-1} = F^{\ell}_{m,NN}$$

where NN is the maximum number of grid points in the z-direction. The distance z_{max} is selected such that the integration domain is large enough that two-dimensional flow is recovered and thus (VI-15) becomes similar to a plane-of-symmetry condition. Lastly, condition (VI-16) is the free-surface boundary condition which is obtained from (V-14) - (V-16) and (V-18). As discussed previously, two of these conditions can be used to eliminate (η_x, η_y). It is convenient to use the kinematic boundary condition (V-14) and the transverse stress condition (V-16) for this purpose. For the present coordinate system this results in

$$\eta_x = [2W(V_y + UK_{21}) - V(V_z + W_y)]/D \qquad \text{(VI-17)}$$

$$\eta_y = [U(V_z + W_y) - WU_y]/D \qquad \text{(VI-18)}$$

where

$$D = 2U(V_y + UK_{21}) - VU_y \qquad \text{(VI-19)}$$

The normal (V-18) and longitudinal (V-15) stress conditions can be solved for (U_z, W_z) which, for the present coordinate system, are given by

$$U_z = U_y \eta_y \qquad \text{(VI-20)}$$

$$W_z = \frac{1}{2}[U_y \eta_y \eta_x + W_y \eta_y] \qquad \text{(VI-21)}$$

Conditions (VI-20) and (VI-21) are implemented in finite-difference form by

$$F^{\ell}_{m,0} = F^{\ell}_{m,1} - \Delta z_o C_3 \qquad \text{(VI-22)}$$

where C_3 is a 2 component column vector composed of the right-hand sides of equations (VI-20) and (VI-21) and n=1 corresponds to the mean water level z = 0. The symmetry-condition boundary condition is obtained by simply putting C_3 = 0 in (VI-22). Due to the highly nonlinear character of (VI-22), it was necessary to use under-relaxation. At the end of each complete ADI sweep, (VI-22) was updated using an under-relaxation factor of .25.

Refering to (VI-17) - (VI-19), it is seen that the evaluation of (η_x, η_y) requires V_y. In order to evaluate V_y correctly it was necessary to account for the grid nonorthogonality in the marching direction. Specifically, in integrating the continuity equation, the following modifications were required:

$$\frac{\partial U}{\partial x} = \frac{\partial U}{\partial x} - \frac{\partial y}{\partial x}\frac{\partial U}{\partial y} \qquad \text{(VI-23)}$$

$$V = V + U \sin \alpha \qquad \text{(VI-24)}$$

where

$$\alpha = \tan^{-1} h_2 K_{21}$$

Similar corrections with respect to z derivatives had been made previously by Baek (1984).

B. Laminar-Flow Results. Laminar-flow calculations were made for Reynolds number $R_n = U_o L/\nu = 20{,}000$. In the discussions to follow, the (x,y,z) coordinates are nondimensionalized based on the plate length L. Both L and the wave length $\lambda = 2\pi/k$ are given the value of one. Typically, 170 x-steps and 21 grid points across the boundary layer were used. An expanding grid was used in the z-direction with 8-15 grid points and $z_{max} = .75$. For the symmetry-condition calculations 8 z-grid points were sufficient with the first point below z = 0 at $z_1 = .025$. The calculations in which the small-amplitude-wave free-surface boundary conditions were used required 12-15 z-grid points and $z_1 = .001$. Numerous checks were made to insure that the results were grid independent. Also, a strict convergence criteria was used, namely

$$\Delta F/Q_e < .00005$$

where $Q_e = \sqrt{U_e^2 + W_e^2}$ and a minimum of three ADI sweeps were required at each cross-plane. The calculations were made on a Prime-750 computer and took from 1-3 hours of computing time depending on the z-grid distribution and the wave

steepness. The Blasius solution based on local R_n was used for the initial conditions.

The results from the symmetry-condition calculations are shown in figures 9 through 13. The results shown are for Ak = (.01,.1,.2,.3). Figure 9 shows a comparison of the streamwise displacement thickness δ^* vs. distance along the plate for each value of Ak. The curves in figure 9 have been normalized using the solution obtained at the greatest depth z_{max} = .75, that is, the Blasius solution. The Blasius solution was recovered at this depth to within a few percent for all the integral parameters and the wall shear stress. The normal velocity component V (VI-24) was only recovered to about ten percent accuracy. Referring to figure 9a, which is for Ak = .01, it is seen that, for x < .15, the displacement thickness is somewhat thicker near the free surface than it is at greater depths. This is no doubt due to the initial conditions and the decrease in local R_n towards the free surface in this potential-flow region (see figure 7). Subsequently, for x > .15, the displacement thickness is reduced near the free surface as compared with greater depths. This reduction is due both to the favorable p_x in potential-flow regions I and II and to the favorable p_z in region I. A favorable p_x tends to accelerate the flow and thin the boundary layer in that region. A favorable p_z tends to drive the cross-flow away from the free surface and thin the boundary layer in that region. The minimum displacement thickness shows about a 3 percent reduction and occurs near x = .45. For x > .45, the displacement thickness near the free surface increases such that for x > .75 it is greater near the free surface than it is at larger depths. This increase is initially due to adverse p_z in potential-flow region II which tends to drive the cross-flow towards the free surface and thickens the boundary layer in that region. This is compounded by continued adverse p_z in potential-flow region III and adverse p_x in regions III and IV. An adverse p_x tends to decelerate the flow and thicken the boundary layer in that region. The maximum displacement thickness shows about a 2.5 percent increase and occurs near x = .86. Lastly, for x > .86, the displacement thickness near the free surface decreases until the end of the plate is reached at x = 1. This reduction is due to the favorable p_z in potential flow region IV. Figures 9b-9d show that the aforementioned trends are greatly intensified due to increasing Ak. Also, flow separation

occurs for these larger Ak values: at x = .725 for Ak = .1; at x = .67 for Ak = .2; at x = .64 for Ak = .3. Flow separation is deemed to occur when the streamwise shear-stress component becomes ≤ 0. Note that, for Ak sufficiently large, the influence of adverse p_z in potential-flow regions II and III causes an earlier and more rapid reduction in displacement thickness near the free surface than that obtained for the lower Ak values (see figures 9c and 9d). The other integral parameters (boundary-layer thickness, momentum thickness, shape parameter) all show similar and consistent trends to those described above for the displacement thickness.

The results for the wall-shear-stress magnitude τ_w and angle β are shown in figures 10 and 11 respectively. The figure 10 format is similar to that of figure 9. Referring to figure 10a, which is for Ak = .01, it is seen that the wall-shear-stress behavior is consistent with the previously described displacement thickness, but in reverse trend. Note that the shear stress responds more quickly, and with greater intensity to changes in the potential flow than the displacement thickness. The maximum and minimum values show about a 7.5 percent and a 10 percent change from the Blasius solution respectively. Referring to figure 11a, which is for Ak = .01, it is seen that the shear-stress angle

$$\beta = \tan^{-1} \lim_{y \to 0} \frac{W}{U}_y$$

can be directly correlated with p_z. In potential-flow region I, where p_z is favorable, β is positive. In regions II and III, where p_z is adverse, β is negative. Finally, in region IV, where p_z is again favorable, β is positive. Note that there is a lag in the β response to p_z such that β becomes negative at $x \approx .325$ and positive again at $x \approx .85$. It should be recognized that β indicates the direction of the cross-flow near y = 0 and it is in this low-inertia region that W first responds to changes in p_z. Thus, subsequent to a sign change in β, so-called S-type cross-flow profiles occur as will be shown next. Also seen from figures 10 and 11 is that increasing Ak greatly intensifies the wall-shear-stress response which is consistent with the displacement-thickness results.

The streamwise velocity profile U along the mean free surface (z=0) at various cross-planes is shown for Ak = .3 in figure 12. In this figure the U profiles have been normalized by U_e and are plotted vs. y/δ. It can be seen that for x = .1 the U profile is similar to the Blasius profile. Subsequently, during the acceleration phase, the U profile is fuller than the Blasius profile, and finally, during the deceleration phase, as separation is approached, it becomes less full. The results for the lower Ak values are similar only with reduced intensity as can be deduced from figure 9. The cross-flow velocity profile W along the mean free surface (z=0) at various cross-planes is shown for each Ak = (.01, .1, .2, .3) in figure 13. In this figure the W profiles have been normalized by Ak and are plotted vs. y/δ. Referring to figure 13a, which is for Ak = .01, it is seen that initially, for x = .1 and .2, the cross-flow is positive. Subsequently, beginning with the inner part of the profile first, the cross-flow becomes negative (x = .5,.6, .7,.8). Lastly, for x = .9 and 1., again beginning with the inner part of the profile first, the cross-flow becomes positive. The influence of increasing Ak on the W profile, as can be seen from figures 13b-13d, is to increase the maximum velocity during the initial phase and decrease the minimum velocity during the subsequent phase. The velocity profiles at greater depths show very similar trends to those just discussed, but with reduced amplitudes in their deviation from the Blasius solution due to the exponential decay of p_x and p_z.

The results from the symmetry-condition calculations were explained solely with reference to the potential-flow pressure field and without regard to the free-surface boundary conditions. This is because the symmetry condition violates the free-surface boundary conditions and basically allows the solution to be continuous through the free-surface. Calculations were also made to investigate the influence of the small-amplitude-wave free-surface boundary conditions (VI-20) and (VI-21). Imposing these highly nonlinear conditions proved to be a severe test of the present computational method. As will now be discussed, in regions where $W > 0$ and U_z (VI-20) was large, the numerics were prone to instability. The results from the calcuations for Ak = .01 are shown in figures 14 and 15. Also discussed are the results obtained for Ak = (.001,.005,.03).

For very small Ak, the behavior of the solution is very similar to that obtained using the symmetry conditions. The maximum deviation from the Blasius solution is only about one percent for Ak = .001. For the larger Ak values investigated, Ak = (.005,.01,.03), the results show a marked influence on the solution due to the change in boundary condition. Figures 14a - 14c show the displacement thickness and wall-shear-stress magnitude and angle, respectively, for Ak = .01. By comparing figures 9a and 10a to 14 it is seen that the differences are only appreciable in the region very close to the free surface $z < Ak$ and for $x < .75$. Specifically, during the acceleration phase (favorable p_x and p_z) a much larger decrease in displacement thickness and increase in wall shear stress is obtained and the minimum and maximum values no longer occur near x = .45 for all depths but vary from x = .275 at z = 0 to x = .45 for $z > .023$. The minimum displacement thickness shows about a 10 percent reduction as compared to the symmetry-condition calculation which only showed a 3 percent reduction. Similarly, the maximum shear stress shows about a 14 percent increase as compared to the symmetry-condition calculation which only showed a 7.5 percent increase (see figure 10a). By comparing figures 11a and 14c, it is seen that the change in boundary condition has no appreciable effect on the wall-shear-stress angle. The calculations for Ak = (.005, .01) became unstable near the free surface for $x > .875$ indicating initially, a rapid thinning of the boundary layer and an increase in the wall-shear stress, followed by large amplitude oscillations. This same type of instablity occurred in the Ak = .03 calcuation only for x = .2; that is, near the location of the minimum displacement thickness. In order to explain the above differences from the symmetry-condition results, including the occurrence of instability, it is necessary to examine the small-amplitude-wave boundary conditions in more detail.

Figures 15a and 15b show the calculated free-surface slopes η_x (VI-17) and η_y (VI-18) for Ak = .01. From figure 15a, it can be seen that η_x deviates somewhat from its potential-flow value $\tan^{-1} W_e/U_e$, especially in the inner part of the boundary layer. It is interesting that the shape of the η_x profile is similar to the W profile. Its magnitude is 0(Ak) as expected. From figure 15b, it can be seen that $\eta_y \to 0$ at the edge of the boundary layer and

becomes large in the inner part***. Initially, for $x \leq .3$, η_y is negative and of small magnitude. Subsequently $x \leq .8$, η_y becomes positive and large. Lastly, η_y becomes negative and very large. The shape of the η_y profile is similar to the -W profile. The free-surface displacement η is obtained from η_y as

$$\eta = - \int_{\delta}^{0} \eta_y dy$$

and is shown in Figure 15c. It can be seen that η basically follows the behavior of W as would be expected , in this case, based on physical reasoning. The small-amplitude-wave boundary conditions U_z (VI-20) and W_z (VI-21) are shown in figures 15d and 15e for Ak = .01. From figure 15d, it is seen that U_z ($= \eta_y U_y$) follows a very similar trend to that of η_y (and - W), but with a greatly increased magnitude. Figure 15e shows that W_z follows a similar trend to that of η_x (and W), but with an increased magnitude, although not nearly so large as U_z. Note that U_z (or W_z) < 0 implies an increase in velocity towards the free surface and U_z (or W_z) > 0 a decrease.

Based on figure 15, the influence of the small-amplitude-wave boundary conditions can be explained as follows. Initially, when $U_z < 0$, the U profile near the free surface is increased, resulting in a larger reduction in displacement thickness and increase in wall shear stress then that obtained due to (p_x, p_z) effects alone. Subsequently, when $U_z > 0$, the U profile near the free surface is decreased at a more rapid rate than that indicated by (p_x, p_z) alone. However, for $x > .45$, the influence of the boundary condition is not appreciable until x = .875 where the calculation becomes unstable. The reason for this is that, within the context of thin-boundary-layer theory and the zone-of-infuence principle, the free-surface boundary condition does not influence the solution when $W < 0$. For $x \geq .875$, W becomes positive again and U_z is very large. Very large U_z caused the numerics to become unstable. For Ak = .03, this occurred during the initial acceleration phase. Note that the

---

*** Consistent with neglecting the menisus boundary layer, η_y was allowed to go to zero at y = 0; the correct limit is $\eta_y = (U_y W_{yy} - U_{yy} W_y)/3U_y W_y$.

occurrence very near the free surface of such large gradients in the z direction implies that diffusion in this direction should not be neglected in this region. Figure 16 shows the Blasius solution boundary-layer thickness vs. distance along the plate for a R_n = 20,000. With the aid of this figure, the magnitude of Ak/ ε for the four values of Ak investigated Ak = (.001, .005, .01, .03) can be ascertained. Recalling that the small-amplitude-wave solution is restricted to $Ak/\varepsilon < 0(1)$, it is seen that the largest Ak value is at the limiting condition.

The above results are consistent with the previous order-of-magnitude estimates in showing that the free surface boundary conditions have a significant influence on the solution in a region very close to the free surface. The results presented show trends that are very consistent with the behavior that would be expected based on physical reasoning. However, these results must be viewed with some caution due to the limitations of both the small-amplitude-wave solution and the use of thin-boundary-layer theory equations and numerics. It appears that the small-amplitude-wave solution is strictly limited to $0(Ak/\varepsilon) < 1$. However, this cannot be judged fully until higher-order effects are included in the governing equations. As discussed previously, a more consistent formulation requires the solution of the partially-parabolic Navier-Stokes equations. In these equations, diffusion is neglected only in the streamwise direction; thus, the pressure field is fully elliptic and the velocity field is elliptic in each cross-plane. Including diffusion in the z-direction should reduce the gradients and smooth the solution somewhat. Also, the boundary condition will play a role even for $W < 0$. Based on the above, it is expected that this would result in a much more rapid thickening of the boundary layer in regions where $W < 0$ and $U_z > 0$. The influence of downstream pressure on the above results is difficult to judge.

VII. TURBULENT FLOW

Consideration is now given to the necessary extensions of the previous laminar-flow analysis to turbulent flow and some of the difficulties encountered are indicated. Here, it will not be possible to determine the order-of-magnitude estimates for region IV with the same degree of certainty as that done for laminar flow in Section V. This is due to the present uncertainties in turbulence modeling, especially when a free surface is present. A brief discussion is included concerning this difficult topic. Also, results from turbulent-flow calculations for the Stokes-wave/flat-plate flow geometry are presented. The results were obtained using the symmetry-condition approximation for the free-surface boundary condition. Thus, no attempt was made to resolve the details of the flow very near the free surface (region IV) and as such a simple modification is made to a one-equation wall turbulence model to account for the influence of the free surface. Of particular interest was the influence of turbulence on the previously discussed laminar-flow symmetry-condition results.

Turbulent-flow analysis will be discussed within the context of the Reynolds equations. The boundary-layer equations for turbulent flow differ from the laminar-flow momentum equations by the additional Reynolds stress terms $\overline{u_i u_j}$. Thus, for turbulent flow, the thin-boundary-layer equations (IV-1) - (IV-3) are supplemented by the following terms respectively

$$\frac{1}{h_2}\frac{\partial}{\partial y}(\overline{uv}) \qquad \text{(VII-1)}$$

$$\frac{1}{h_2}\frac{\partial}{\partial y}(\overline{v^2}) \qquad \text{(VII-2)}$$

$$\frac{1}{h_2}\frac{\partial}{\partial y}(\overline{vw}) \qquad \text{(VII-3)}$$

The more complete partially-parabolic Reynolds equations contain all six Reynolds stresses. Closure of the Reynolds equations requires the use of a turbulence model, as will be discussed subsequently. First, the modifications of the free-surface boundary conditions and the small-amplitude-wave solution for turbulent flow are considered.

For turbulent flow, the fluid stress (IV-13) is given by

$$\tau_{ij} = - p \delta_{ij} + 2\mu\varepsilon_{ij} - \rho \overline{u_i u_j} \qquad \text{(VII-4)}$$

and consequently the dynamic boundary condition (IV-9) becomes

$$p\eta_x - (2\mu a - \rho\overline{u^2})\eta_x - (\mu h - \rho\overline{uv})\eta_y + \mu g - \rho\,\overline{uw} = (p_o - p_\gamma)\,\eta_x \qquad \text{(VII-5)}$$

$$p\eta_y - (\mu h - \rho\overline{uv})\eta_x - (2\mu b - \rho\overline{v^2})\,\eta_y + \mu f - \rho\,\overline{vw} = (p_o - p_\gamma)\,\eta_y \qquad \text{(VII-6)}$$

$$- p - (\mu g - \rho\,\overline{uw})\eta_x - (\mu f - \rho\overline{vw})\eta_y + 2\mu c - \rho\overline{w^2} = - (p_o - p_\gamma) \qquad \text{(VII-7)}$$

The kinematic boundary condition (IV-16) is unchanged

$$- \eta_x U - \eta_y V + W = 0 \qquad \text{(VII-8)}$$

In principle, if the Reynolds stresses are known, conditions (VII-5) - (VII-8) can be treated in a similar manner as they were for laminar flow; that is, (VII-6) and (VII-8) can be used to eliminate η_x and η_y in (VII-5) and (VII-7) which can then be used as boundary conditions for the mean-flow momentum equations. At this juncture, it should be pointed out, that additional free-surface boundary conditions may be required in the turbulence-model equations.

For laminar flow, it was possible to determine order-of-magnitude estimates for region IV and, as a result, appropriate simplifications of the free-surface boundary conditions for small-amplitude-waves and different solution regimes were identified. A smilar analysis is not possible for turbulent flow due to the present uncertainty of the order-of-magnitude of the Reynolds stresses $\overline{u_i u_j}$ near a free surface. Often, in three-dimensional boundary layer analysis it is assumed that

$$\overline{u_i u_j} \sim 0(\varepsilon) \qquad \text{(VII-9)}$$

and can be represented by an isotropic eddy viscosity

$$- \overline{u_i u_j} = 2\,\nu_t\,\varepsilon_{ij} - 1/3\,\overline{q^2}\,\delta_{ij} \qquad \text{(VII-10)}$$

where $\overline{q^2} = \overline{u^2} + \overline{v^2} + \overline{w^2}$ is the turbulent kinetic energy and ν_t the turbulent eddy-viscosity. If these assumptions are made for the present problem, identical conclusions to those reached for laminar flow in Section V can be reached for turbulent flow as well. However, assumptions (VII-9) and (VII-10) are not directly applicable to the present problem; since, the complex effects described earlier that a free surface has on a turbulent flow cannot be simulated with an isotropic eddy-viscosity turbulence model. Tentatively, based on physical reasoning, it is assumed that conclusions similar to those reached for laminar flow for region IV can also be extended to turbulent flow. That is, for Ak/ε of sufficient magnitude, the flow in region IV should be treated as partially parabolic and a small-amplitude-wave solution in which the free-surface boundary conditions are applied on the mean free-surface, is restricted to small Ak/ε. More definitive conclusions can only be reached when further experimental and numerical work is done.

A turbulence model is required that includes modeling of the individual Reynolds stresses and/or a nonisotropic eddy-viscosity. Rodi (1980) and Celik et al (1982) have developed a turbulence model for open channel flow that includes free surface effects. In their approach, the k-ε turbulence model is modified to include a nonisotropic turbulent eddy-viscosity which is determined based on algebraic expressions derived for the individual Reynolds stresses. Also, the length scale is reduced near the free surface through the ε free-surface boundary condition. The results show favorable agreement with experimental data; however, the authors point out that the procedure is only tentative and needs both further numerical testing and experimental validation. The influence of streamline curvature and the presence of a surface-piercing body is not known. The turbulence model just described can be extended for application to the present problem; however, this is beyond the scope of the present investigation and recommended for future study.

A. Computational Method

If the turbulent motion is characterized by a single length scale, then it is expected that this scale must decrease towards a free surface due to geometrical restrictions. In the present investigation, a simple modification

is made to a one-equation wall-turbulence model to account for the influence of the free surface. This is consistent with the use of the symmetry-condition boundary condition.

Specifically, the Bradshaw/Nash one-equation turbulence model, which was built into the original Nash and Scruggs (1976) program, was used here also. In this procedure, an approximate form of the turbulent kinetic energy equation is solved in conjunction with the boundary-layer equations. The turbulent-kinetic-energy equation is put in the form

$$\frac{U}{h_1}\frac{\partial}{\partial x}(\overline{q^2}/2) + \frac{V}{h_2}\frac{\partial}{\partial y}(\overline{q^2}/2) + \frac{W}{h_3}\frac{\partial}{\partial y}(\overline{q^2}/2) + \frac{\overline{uv}}{2}\frac{1}{h_2}\frac{\partial U}{\partial y} + \frac{\overline{vw}}{2}\frac{1}{h_2}\frac{\partial w}{\partial y} + D - \varepsilon = 0 \qquad \text{(VI-11)}$$

where

$$D = \frac{1}{h_2}\frac{\partial}{\partial y}\left(\frac{\overline{pv}}{\rho} + \frac{\overline{q^2 v}}{2}\right) \qquad \text{(VI-12)}$$

$$\varepsilon = \nu\left[2\overline{\nabla^2 u} + \overline{v\nabla^2 v} + \overline{w\nabla^2 w}\right] \qquad \text{(VI-13)}$$

The diffusion term (VII-12) is represented by a bulk diffusion model

$$D = \frac{1}{h_2}\frac{\partial}{\partial y}\left[\frac{\overline{q^2}_{max}}{Q_e} a_2 \overline{q^2}\right] \qquad \text{(VII-14)}$$

where

$\overline{q^2}_{max}$ = maximum value of $\overline{q^2}$ in the outer 3/4 of δ

$$a_2 = 1.125\,(y/\delta)^2 - .375\,(y/\delta)^4$$

The dissipation term (VII-13) is represented by

$$\varepsilon = (\overline{q^2})^{3/2}/L_D \qquad \text{(VII-15)}$$

where L_D is the dissipation length

$$L_D = 7.195\ \eta/(1 + 4\ \eta^2 + 5\ \eta^7) \qquad \text{(VII-16)}$$

and η is the minimum distance of either y/δ or z/δ. Lastly, the Reynolds stresses are related to the turbulent kinetic energy by the empirical functions

$$\begin{aligned} \rho\ \overline{uv} &= -\ .0225\ \sqrt{\overline{q^2}}\ L_D\ \frac{1}{h_2}\ \frac{\partial U}{\partial y} \\ \rho\ \overline{vw} &= -\ .0255\ \sqrt{\overline{q^2}}\ L_D\ \frac{1}{h_2}\ \frac{\partial W}{\partial y} \end{aligned} \qquad \text{(VII-17)}$$

The turbulent-kinetic-energy equation (VII-11) was solved in conjunction with the mean-flow momentum equations using the ADI procedure as described in Section VI.A with $F^T = (U,W,\overline{q^2})$. For turbulent flow, a nonuniform distribution of grid points is used across the boundary layer in which a higher concentration of grid points is placed near the wall.

B. Turbulent-Flow Results. Turbulent-flow calculations were made for $R_n = 5 \times 10^6$. The calculations were begun as laminar flow, with transition specified at $x = .05$ ($R_{n_x} = 250{,}000$). The same grid distribution and initial conditions as described for the laminar-flow results were used.

The results are shown in figures 17 through 23. The same format is used in figures 17 through 23 as that described earlier for the laminar-flow results. The results shown are for Ak = (.01,.2,.3,.35). Figure 33 shows the displacement thickness. Figure 18 shows the maximum turbulent kinetic energy in the outer 3/4 of δ and is normalized using the solution obtained at the greatest depth $z_{max} = .75$. Figures 19 and 20 show the wall-shear-stress magnitude and angle. Figures 21 and 22 show the (U,W) velocity profiles along the mean free-surface. Lastly, the turbulent-kinetic-energy profiles $\overline{q^2}$ along the mean free surface are shown in figure 23. In this figure the $\overline{q^2}$ profiles have been nondimensionalized by the edge velocity magnitude Q_e^2. The U and turbulent-kinetic-energy profiles are shown for Ak = .3 only.

Scrutiny of the above figures shows that the turbulent-flow results are completely consistent with the symmetry condition laminar-flow results described earlier. The primary influence of the turbulence is to dampen the

three-dimensionality of the flow; that is, the cross-flow is reduced. This reduction in cross-flow inhibits the occurrence of separation such that separation occurs only for the largest Ak value.

Referring to figure 23, which shows the turbulent-kinetic-energy profile along the mean free surface (z=0) at various cross-planes and for Ak = .3, it is seen that initially, during the acceleration phase, the maximum value occurs very close to the wall. Subsequently, during the deceleration phase, the maximum value occurs towards the middle of the boundary layer. This result is consistent with figure 18. By comparing figure 18 with figures 17 and 20, it is seen that the magnitude of the turbulent kinetic energy in the outer 3/4 of δ correlates closely with the wall-shear-stress angle and not the displacement thickness.

VIII. SUMMARY

Through the use of both flow-field order-of-magnitude analysis and three-dimensional thin-boundary-layer calculations for the idealized geometry of a combination Stokes-wave/flat-plate, it has been shown that the influence of free-surface waves on boundary-layer development for surface-piercing bodies can be significant. There are two distinct mechanisms for this influence: the external-flow pressure gradients; and the viscous-fluid free-surface boundary conditions.

The influence of the external-flow pressure gradients is shown to penetrate to a depth on the order of half the wave length, $z \leq \lambda/2 \approx 10\ \delta$. The magnitude of this influence depends on the wave steepness Ak. The symmetry-condition calculations discussed in Sections VI.B for laminar flow and VII.B for turbulent flow demonstrate many interesting effects on the flat-plate boundary-layer development due to a wavy free surface. In particular, it has been shown how the boundary layer responds to the pressure-gradient changes along the plate length between favorable and adverse. Also, waves of sufficient steepness induce flow separation near the free surface in regions of large adverse pressure gradients p_x. The overall influence of turbulence is to dampen the three-dimensionality of the flow and inhibit the occurrence of separation. The symmetry boundary condition is similar to a small-cross-flow boundary condition and as such violates the free-surface boundary conditions.

The influence of the viscous-fluid free-surface boundary conditions is shown to be significant only in a region very close to the free surface $z \leq Ak \approx \delta$. Within this region, order-of-magnitude analysis for laminar flow shows that the parameter Ak/ε is important in characterizing the flow. Only for small $Ak \sim 0(\varepsilon^{1.5})$ or less are the free-surface boundary conditions of higher order. This is the small-cross-flow regime. For larger values of $0(\varepsilon^{1.5}) < Ak < 0(\varepsilon)$ the role of the free-surface boundary conditions is significant; furthermore, a consistent formulation requires the solution of the partially-parabolic Navier-Stokes equations. For this regime, a small-amplitude-wave solution is derived. In this solution the highest-order terms in the free-surface boundary conditions are retained and applied on the mean free surface. The latter approximation is the most severe. For $Ak \leq 0(\varepsilon)$, the small-amplitude-wave solution is no longer valid and the free-surface boundary conditions must be applied on the exact viscous-flow free surface. For turbulent flow, it is not possible to reach such definitive conclusions concerning the order-of-magnitude estimates and solution regimes for region IV. Tentatively, based on physical reasoning, the above conclusions are extended to turbulent flow also.

Calculations were also made for laminar flow to investigate the influence of the small-amplitude-wave free-surface boundary conditions. The results are consistent with the order-of-magnitude analysis in showing that the influence is significant only in a region very close to the free-surface $z \leq Ak \approx \delta$. The results show interesting trends that are explained by reference to the free-surface boundary conditions. It is shown that, within the boundary layer, the potential-flow free surface is deformed in a manner that correlates closely with the cross-flow velocity. In fact, all the small-amplitude-wave free-surface properties are shown to correlate with $\pm W$. Of particular interest is the behavior of the imposed free-surface velocity gradients U_z and W_z. In regions where U_z (or W_z) < 0, there is an increase in velocity towards the free surface, and where U_z (or W_z) > 0 , a decrease. It is shown that the behavior of U_z is similar to $-W$ and W_z to W itself. During the initial acceleration phase, where $W > 0$ we have $U_z < 0$, which results in an even larger acceleration near the free surface than indicated from the symmetry-condition calculations. Subsequently, U_z changes sign, as does W, which

results in an even larger deceleration near the free surface than indicated by the symmetry-condition calculations. However, within the context of thin boundary-layer theory and the zone-of-influence principle, the free-surface boundary conditions do not influence the solution when $W < 0$. Thus, in the present calculations, the influence of the free-surface boundary condition is not well represented for $U_z > 0$.

Imposing the highly nonlinear free-surface boundary conditions proved to be a severe test of the present computation method. In regions where $W > 0$ and U_z was large the numerics were prone to instability. The results presented show trends that are very consistent with the behavior that would be expected based on physical reasoning. However, these results must be viewed with some caution due to the limitations of both the small-amplitude-wave solution and the use of thin-boundary-layer theory equations and numerics. it appears that the small-amplitude-wave solution is strictly limited to $Ak/\varepsilon < 0(1)$. However, this cannot be judged fully until higher-order effects are included in the governing equations. As discussed previously, a more consistent formulation requires the solution of the partially-parabolic Navier-Stokes equations. In these equations diffusion is neglected only in the streamwise direction; thus, the pressure field is fully elliptic and the velocity field is elliptic in each cross-plane. Including diffusion in the z direction should reduce the gradients and smooth the solution somewhat. Also, the boundary condition will play a role even for $W < 0$. Based on the above, it is expected that this would result in a much more rapid thickening of the boundary layer in regions where $W < 0$ and $U_z > 0$. The influence of downsteam pressure on the above results is difficult to judge.

IX. IMPLICATIONS FOR SHIP BOUNDARY LAYERS

The present study has several implications with regard to calculating boundary layers on actual ship forms. Ship boundary layers are fully turbulent over most of their length excluding a small bow region. The Reynolds number is very large which implies very small $\varepsilon = \delta/L \sim 0(10^{-3})$. The wave steepness can very greatly depending on Froude number. Recently, Fei (1984) calculated the wave potential flow around a variety of ship forms using

a Hess-Smith-Dawson method. His results indicate that usually $Ak \leq .1$ except near the bow where it can be considerably larger. Thus, the parameter Ak/ε for ships will typically be fairly large and in some cases $> 0(1)$. The present investigation indicates that the influence of free-surface waves is significant.

For many practical applications it may not be necessary to resolve the flow in the region very close to the free surface ($z < \delta$); consequently, as a first approximation, the boundary layer can be calculated using the symmetry boundary condition and the thin boundary layer equations (except near the stern). In this case, the influence of free-surface effects on the turbulence model should not be significant. However, in order to calculate ship boundary layers, including the region very close to the free surface and the free-surface boundary conditions, the flow must be treated as partially parabolic over the entire length and not just in the thick stern boundary-layer region. Furthermore, in some cases, the small-amplitude-wave solution will not be applicable and it will be necessary to satisfy the free-surface boundary conditions on the exact viscous-flow free surface which must be determined as part of the solution. However, the small-amplitude-wave solution should be useful in this regard. Also, a turbulence model is required that can simulate the influence of a wavy free-surface on the turbulence characteristics.

A number of iterative solution procedures have been developed for solving the partially-parabolic equations (for example, Pratrap and Spalding 1976 and Mahgoub and Bradshaw 1977). The major added difficulties in solving these equations are: 1) computational grid generation; 2) velocity/pressure field coupling procedure; 3) and in regions where the boundary layer is thick either a viscous/inviscid interaction procedure or a large solution domain must also be included. Considerable success with these difficulties has been attained over the last eight years as seen in recent publications (for example, Chen and Patel 1984). For the present application a number of extensions are necessary. In the cases where the free-surface boundary conditions are to be applied on the exact viscous-flow free surface a boundary-fitted coordinate grid generation method will be required. Also, an iterative method for adjusting the free surface such that the free-surface boundary conditions are satisfied will need to be developed.

REFERENCES

Adee, B.H., 1972, "Boundary Layers on Ships", Ph.D. thesis, Univ. of Calif., Berkeley, CA, 56 pp.

Adee, B.H., 1975, "Fluid Flow Around a Ship's Hull", in Proc. 1st Int. Conf. Numer. Ship Hydrodyn., Bethesda, MD, pp. 435-454.

Baek, J-H., 1984, "Three-Dimensional Turbulent Boundary Layers on the Bodies of Revolution at Incidence", Ph.D. thesis, Univ. of Iowa, Iowa City, Iowa.

Celik, I., Rodi, W. and Hossain, M.S., 1982, "Modelling of Free-Surface-Proximity Effects on Turbulence", Proc. Refined Modelling of Flows, Paris.

Chen, H.C. and Patel, V.C., 1984, "Calculation of Stern Flows by a Time-Marching Solution of the Partially-Parabolic Equations" 15th ONR Symposium on Naval Hydrodynamics, Hamburg.

Chow, S.K., 1967, "Free-Surface Effects on Boundary-Layer Separation on Vertical Struts", Ph.D. Dissertation, The University of Iowa.

Doi, Y., 1980, "Observation of Stern Wave Generation", Proc. Continued Workshop on Ship Wave Resistance, Izu Shuzenji, Japan.

Fei, 1984, "Calculation of Potential Flow with a Free Surface", Chalmers U. of Tech. Dept. of Ship Hydro. Report, Gothenburg.

Gadd, G.E., 1971, "The Approximate Calculation of Turbulent Boundary Layer Development on Ship Hulls", Trans. R. Inst. Nav. Archit., 113:59-71.

Hinatsu, M. and Takeshi, H., 1985, "A Calculation Method for Resistance Prediction Including Viscid-Inviscid Interaction", Proc. 2nd Sym. Ship Viscous Resistance, Goteborg.

Hotta, T. and Hatano, S., 1983, "Turbulence Measurements in the Wake of a Tanker Model on and under the Free Surface", read at the Autumn Meeting of the Society of Naval Architects of Japan.

Huang, T.T. and von Kerczek, C., 1972, "Shear Stress and Pressure Distribution on a Surface Ship Model: Theory and Experiment", Ninth symposium of naval Hydrodynamics, paris, France.

Kinsman, B. 1976, "Wind Waves", Prentice-Hall, Englewood Cliffs.

Lin, J.D. and Hall, R.S., 1966, "A Study of Flow Past a Ship-Like Body", Univ. Conn C.E. Dept. Rep. CE-66-7, 130 pp.

Mahgoub, H.E.H. and Bradshaw, P., 1977, "Calculation of Turbulent-Inviscid Flow Interactions with Large Normal Pressure Gradients", A.R.C. 37 572.

Mei, C.C. 1983, "The Applied Dynamics of Ocean Surface Waves", John Wiley & Sons, New York.

Nagamatsu, T. 1981, "Flow Measurements Near the Stern of a Model of a Full Form Ship", Proc. 30th Japan nat. Congress for Appl. Mech., Vol. 30, pp. 481-492.

Nash, J.F. and Patel, V.C., 1972, "Three Dimensional Turbulent Boundary Layers", SBC Tech books, Atlanta.

Patel, V.C. and Choi, D.H., 1979, "Calculation of Three-Dimensional Laminar and Turbulent Boundary Layers on Bodies of Revolution at Incidence", Proc. 2nd Sym. Turbulent shear Flow, London, pp. 179-217.

Patel, V.C. 1982, "Some Aspects of Thick Three-Dimensional Boundary Layers", Proc. 14th ONR Sym. Naval Hydrodynamics, Ann Arbor, MI, pp. 999-1040.

Patel, V.C., Sarda, O.P. and Shahshahan, A., 1983, "Calculation of Ship Boundary Layers", Proc. 4th Sym. Turbulent Shear Flow, Karlsruhe, p. 3.1.

Patel, V.C. and Baek, J.H., 1983, "Calculation of Boundary Layers and Separation on a Spheroid at Incidence", Proc. 2nd Sym. Numerical & Physical Aspects of Aerodynamic Flows, Long Beach, CA; Also, AIAA JOurnal, Vol. 23, pp. 55-63, 1985.

Pratap, V.S. and Spalding, D.B., 1976, "Fluid Flow and Heat Transfer in Three-Dimensional Duct Flows", J. of Heat and Mass Transfer, Vol. 29, pp. 1183-1188.

Rodi, W., 1980, "Turbulence Model and Their Application in Hydraulics" presented at the IAHR-Section on Fundmentals of Division II: Experimental and Mathematical Fluid Dynamics.

Sachdeva, R.C. and Preston, J.H., 1975, "Theoretical Calculation of Boundary Layers on Ship Hulls", Trans. N.E. Coast Inst. Eng. Shipbld. 92:17-22.

Salvesen, N., von Kerczek, C.H., Yue, D.K. and Stern, F., "Computations of Nonlinear Surge Motions of Tension Leg Platforms", OTC Paper #4394, 14th Annual Offshore Technology Conference, Houston, TX, May 1982, pp. 199-215.

Sarpkaya, T. and Isaacson, M., 1981, "Mechanics of Wave Forces on Offshore Structures", Van Nostrand Reinhold Company, New York.

Shahshahan, A. and Patel, V.C., 1983, "The Boundary-Layer at Hull-Wave Intersections", 18th Midwestern Mech. Conf., Iowa City, Iowa.

Steele, B.N., 1967, "Measurements of Components of Resistance on a Tanker Model", National Physical Laboratory Ship Division Report No. 106.

Steele, B.N. and Pearce, G.B., 1968, "Experimental Determination of the Distribution of Skin Friction on a Model of a Shigh Speed Linear", Transactions of Royal Institution of Naval Architects Vol. 110, p. 79.

Tzou, K.T.S., 1968, "An Experimental Study of Shear Stress Variation on Series-60 Ship Model", Iowa Institute of Hydraulic Research Report No. 108.

Webster, W.C. and Huang, T.T., 1979, "Study of the Boundary Layer on Ship Forms", J. Ship Research, Vol. 14, pp. 153-167.

Wu, J. and Landweber, L. 1963, "Variation of Viscous Drag with Froude Number", Proc. 10th Int. Towing Tank Conf., 2:90-95.

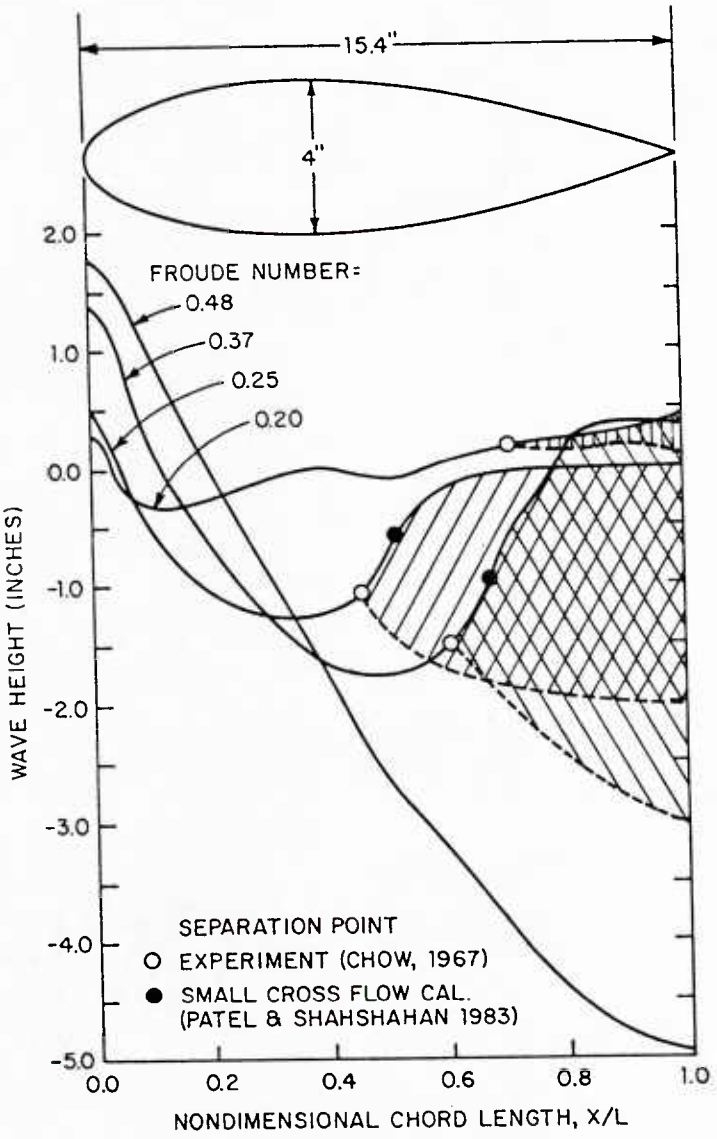

Figure 1. Experimental Wave-Induced Separation (Chow 1967)

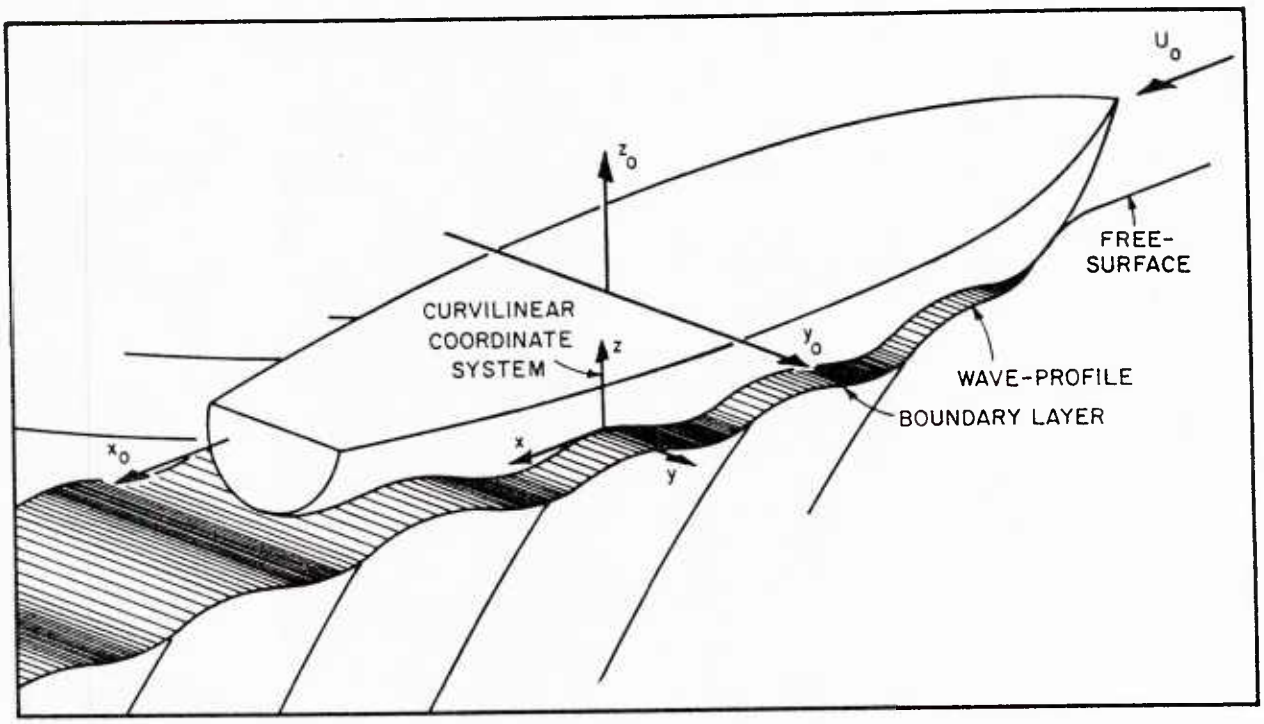

Figure 2. Definition Sketch

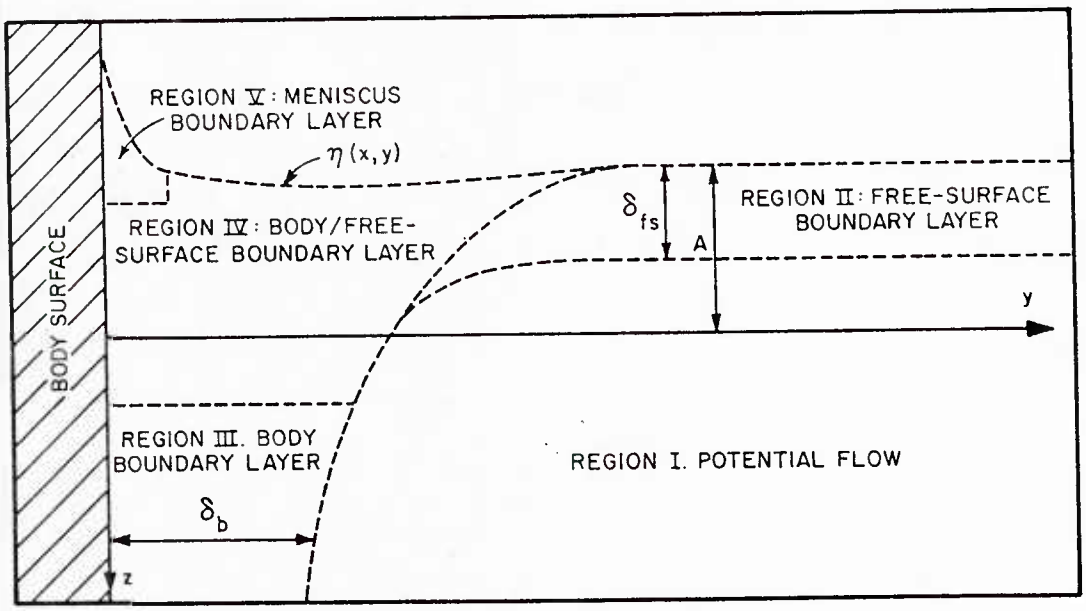

Figure 3. Flow Field Region Definition Sketch

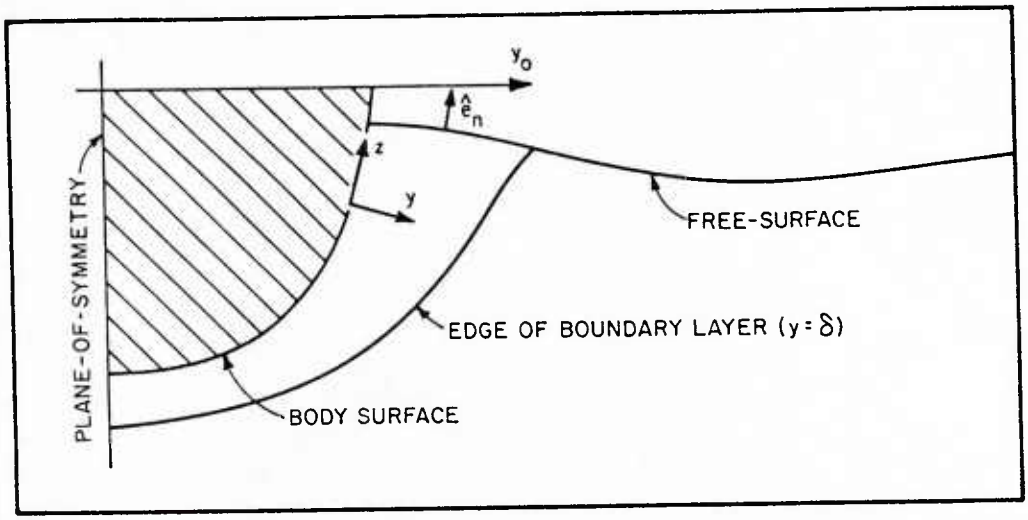

Figure 4. Projection of x = Constant Surface onto Body Cross-Section Plane

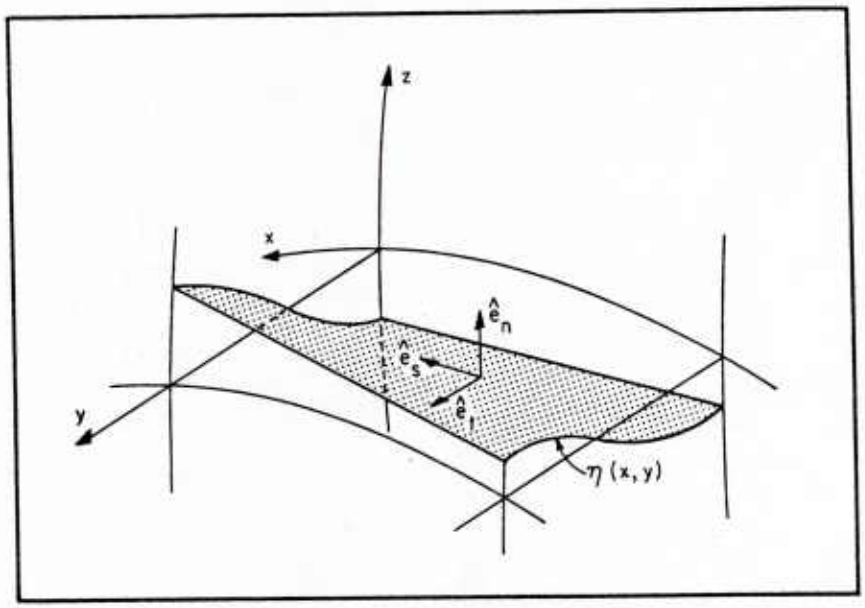

Figure 5. Free-Surface Deformation within the Boundary Layer η (x,y)

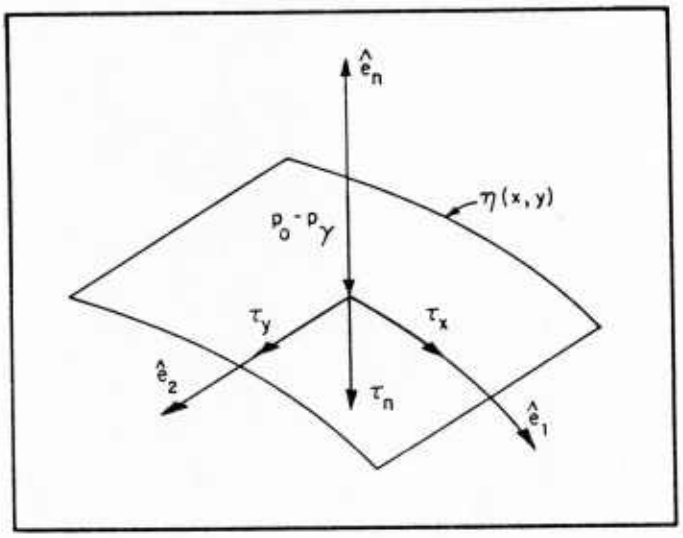

Figure 6. Dynamic Free-Surface Boundary Condition

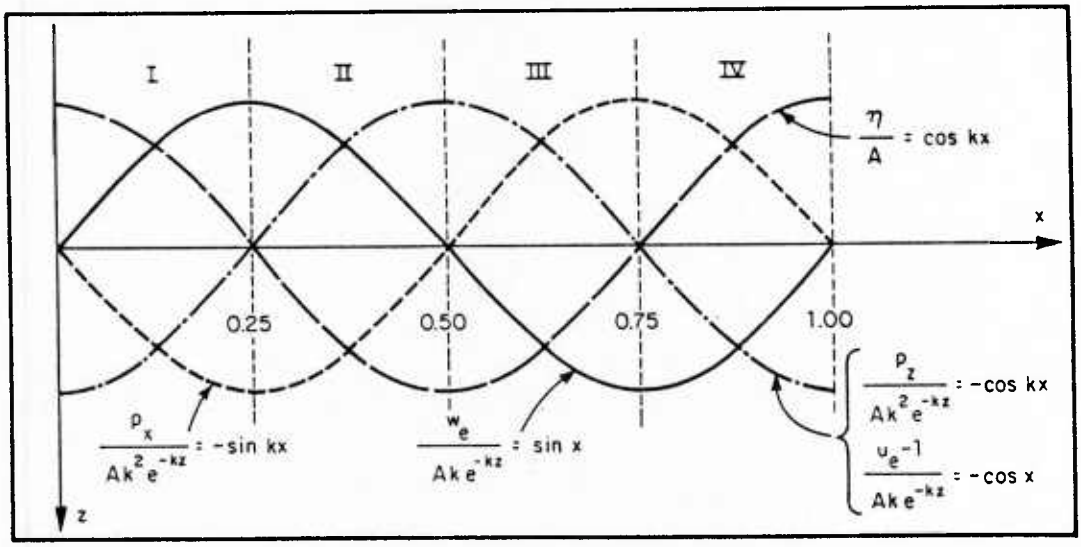

Figure 7. Potential-Flow Regions Definition Sketch

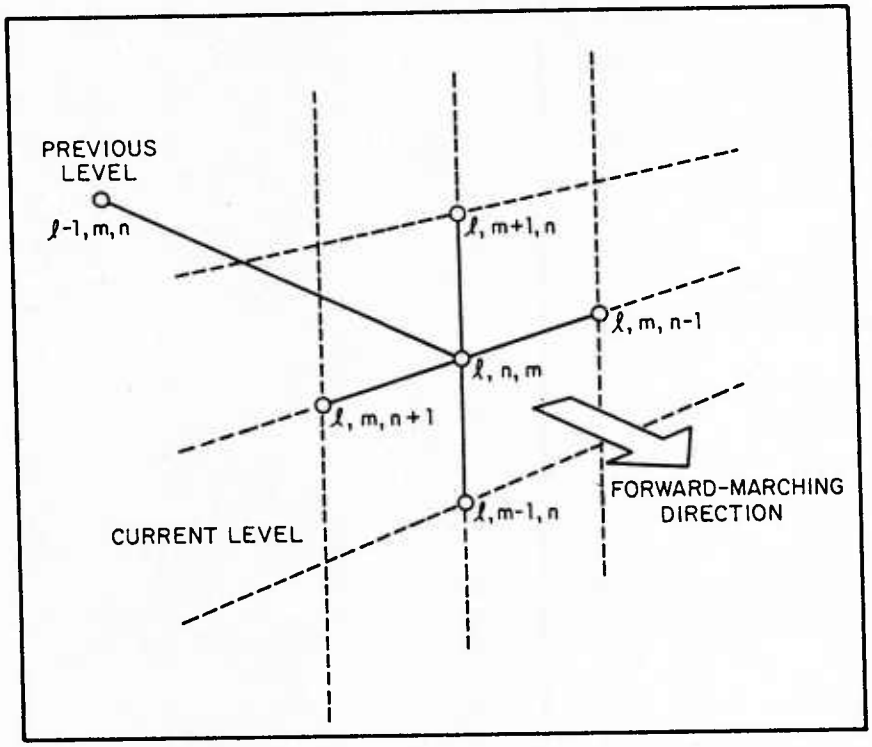

Figure 8. Finite-Difference Molecule

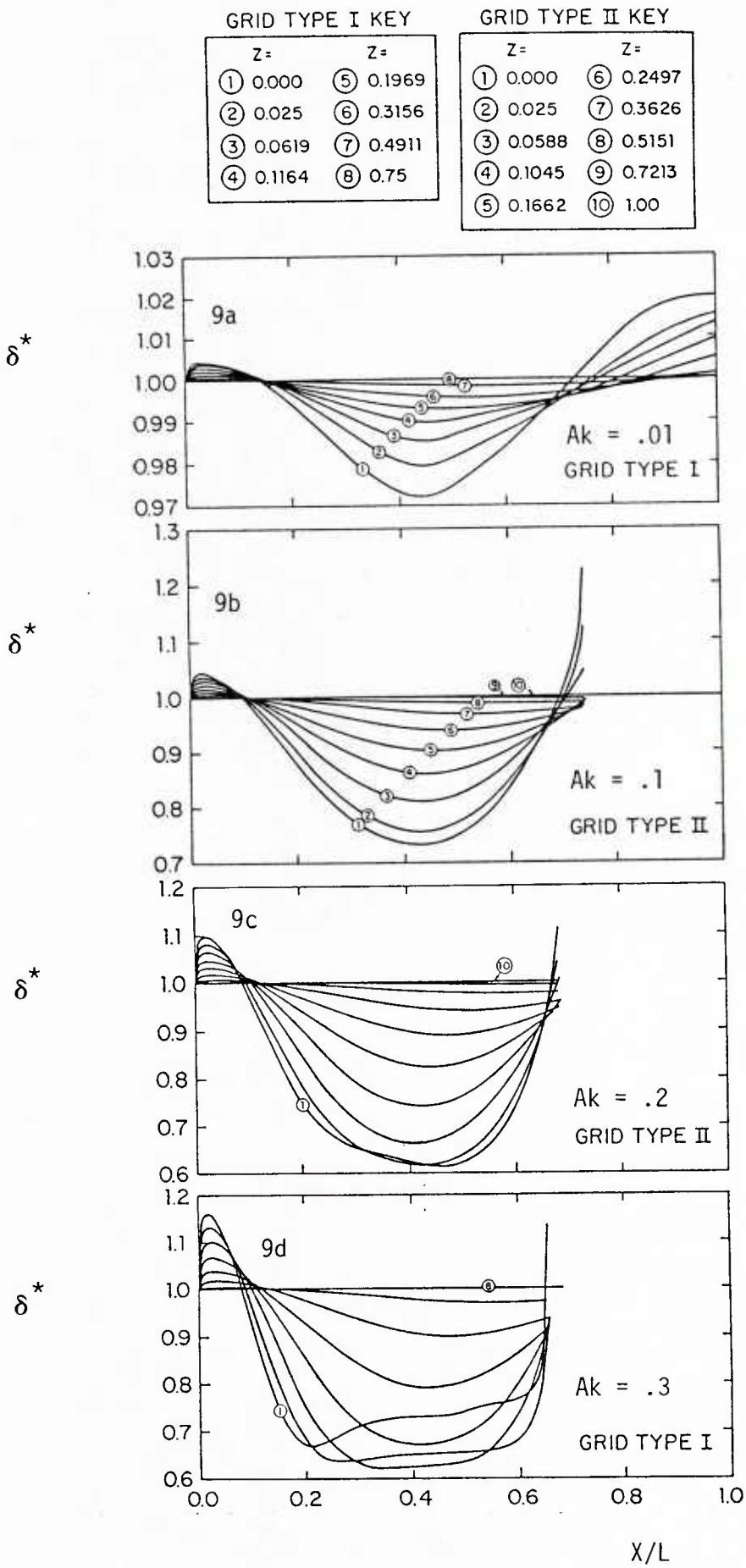

Figure 9a-d. Normalized Displacement Thickness δ^*

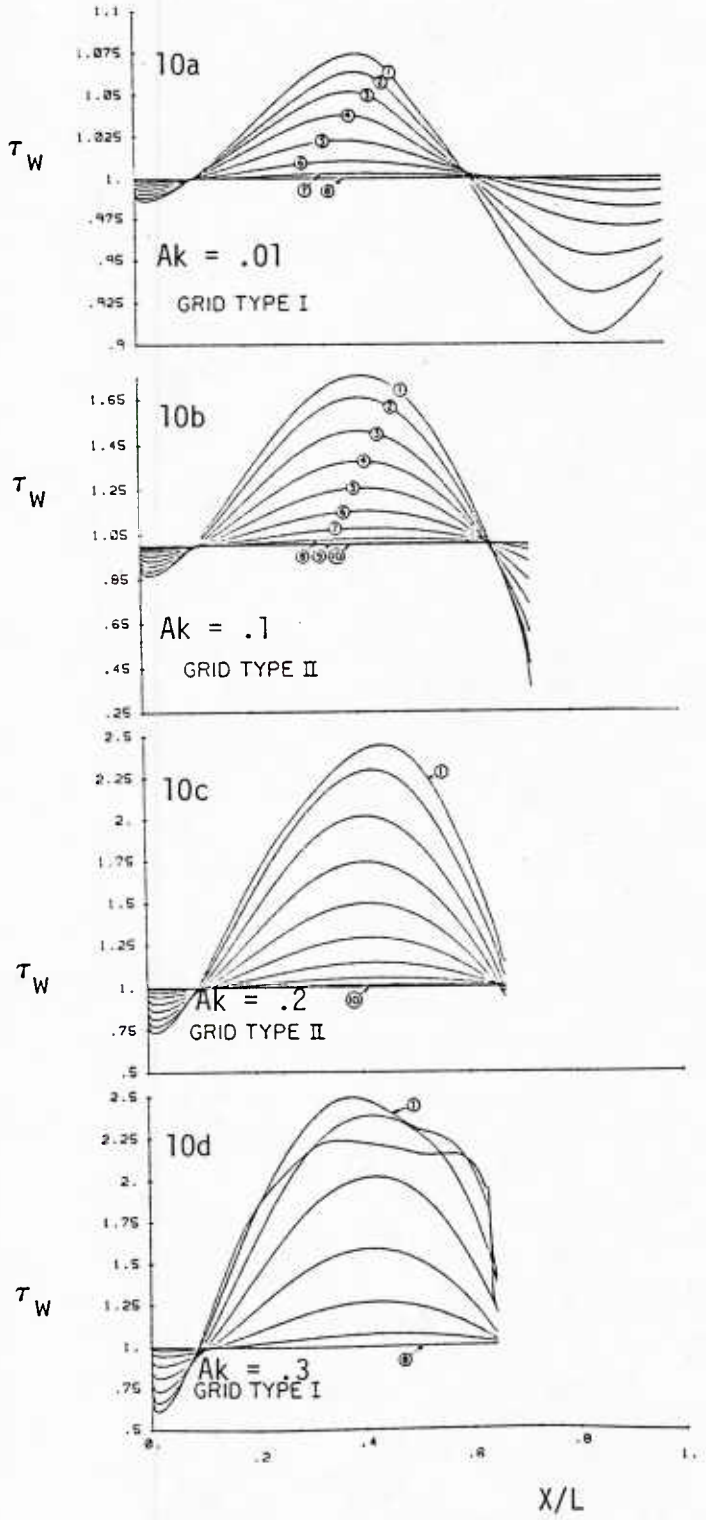

Figure 10a-d. Normalized Wall-Shear-Stress Magnitude τ_w

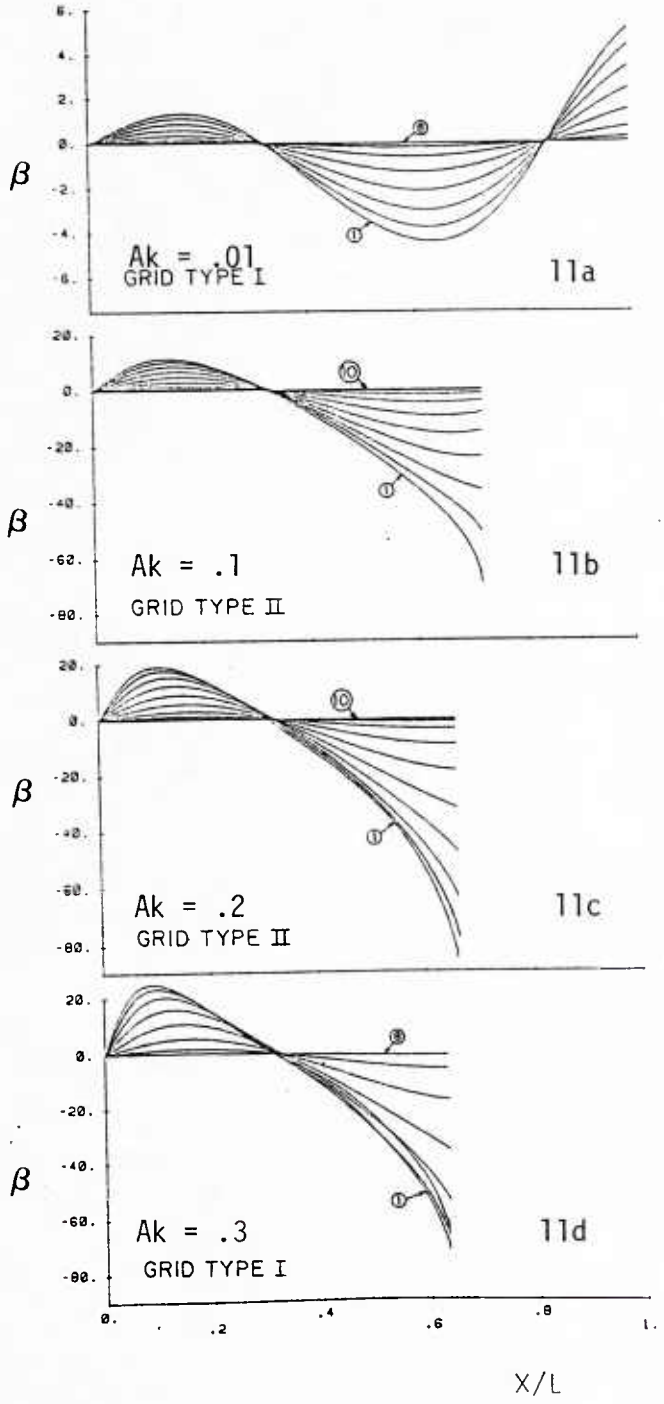

Figure 11a-d. Wall-Shear-Stress Angle β (Degrees)

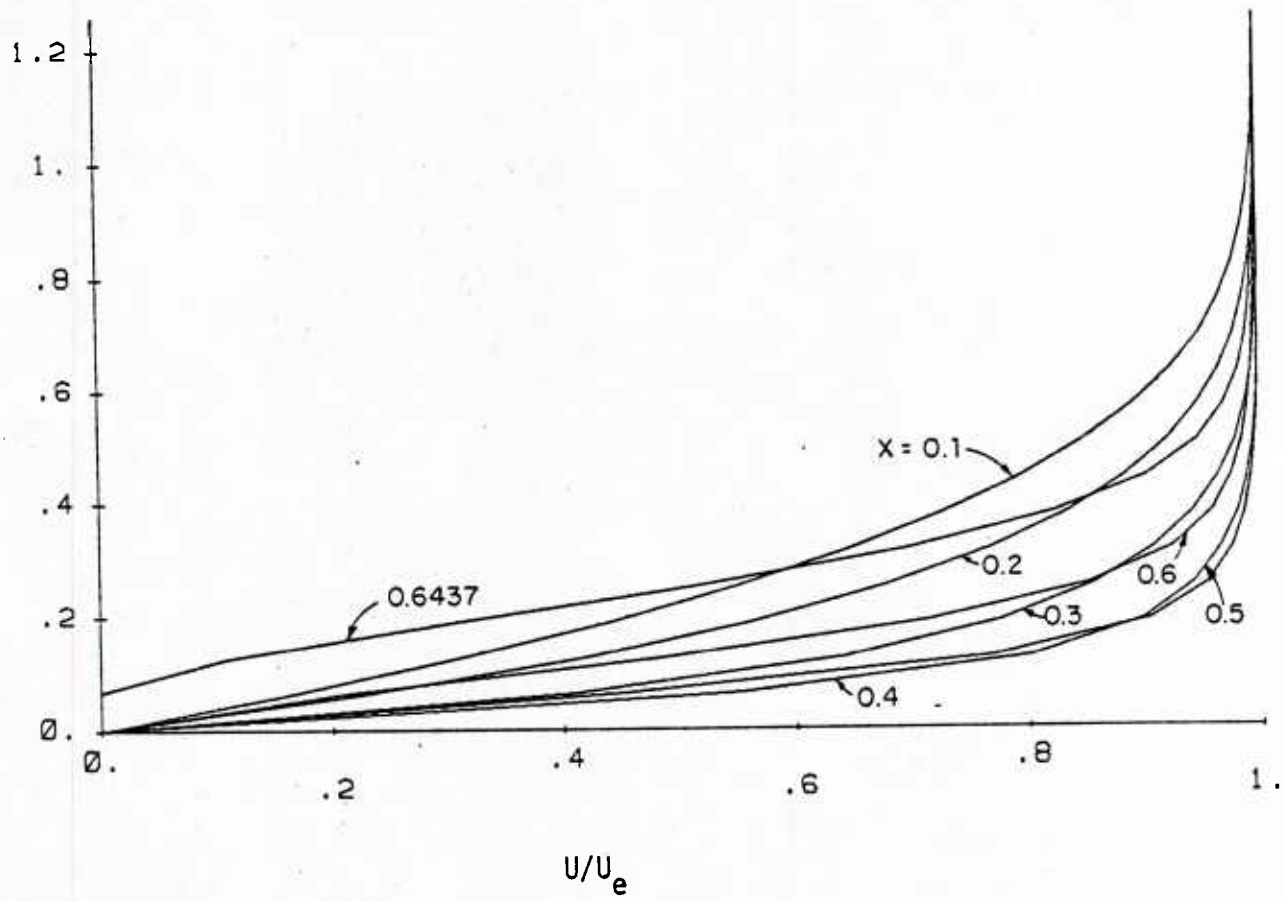

Figure 12. Streamwise Velocity Profile U/U_e Along the Mean Free Surface (z=0) at Various Cross-Planes: Ak=.3

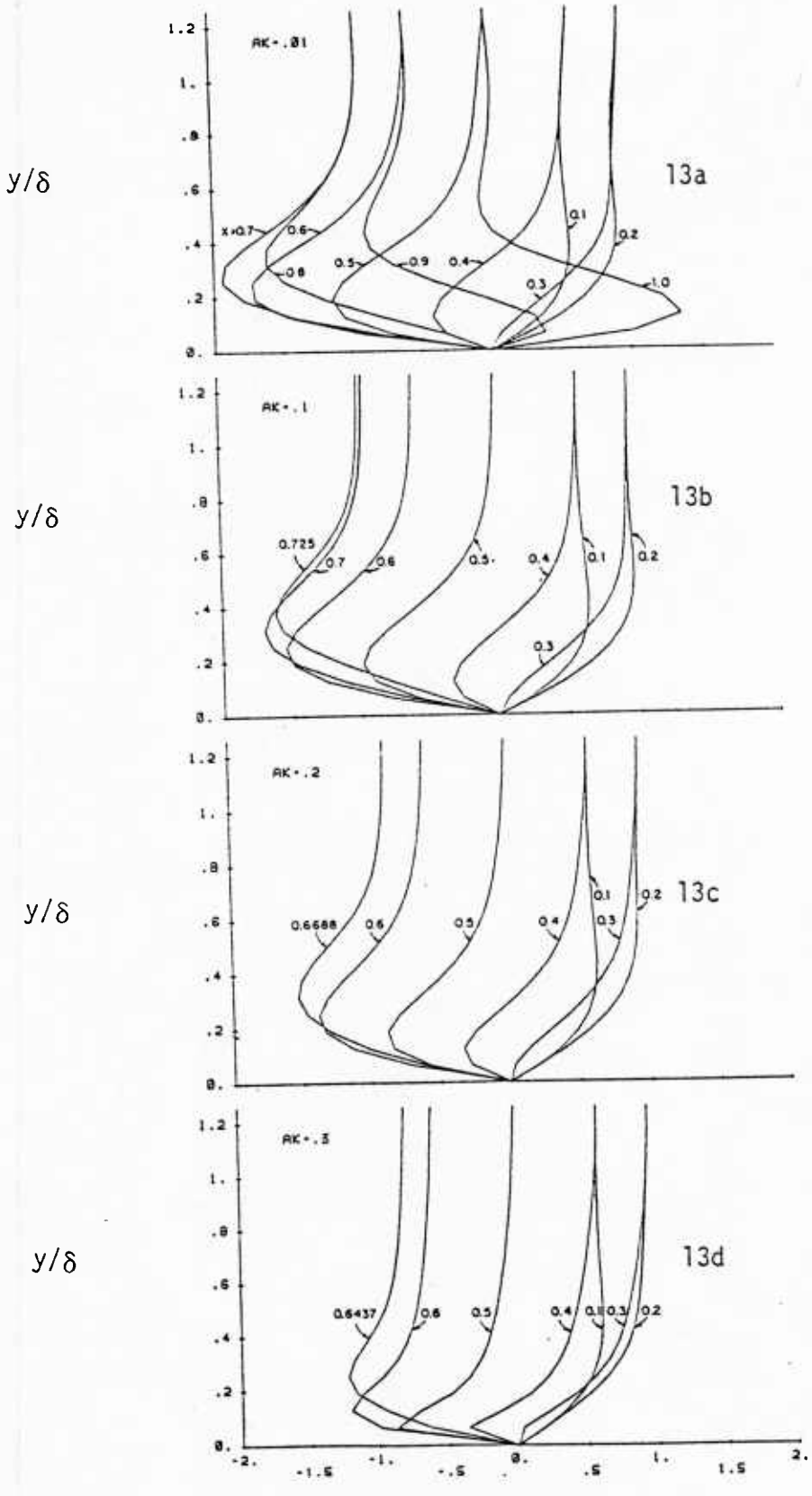

Figure 13a-d. Cross-flow Velocity Profile W/Ak Along the Mean Free Surface (z=0) at Various Cross-Planes: Ak= (.01, .1, .2, .3)

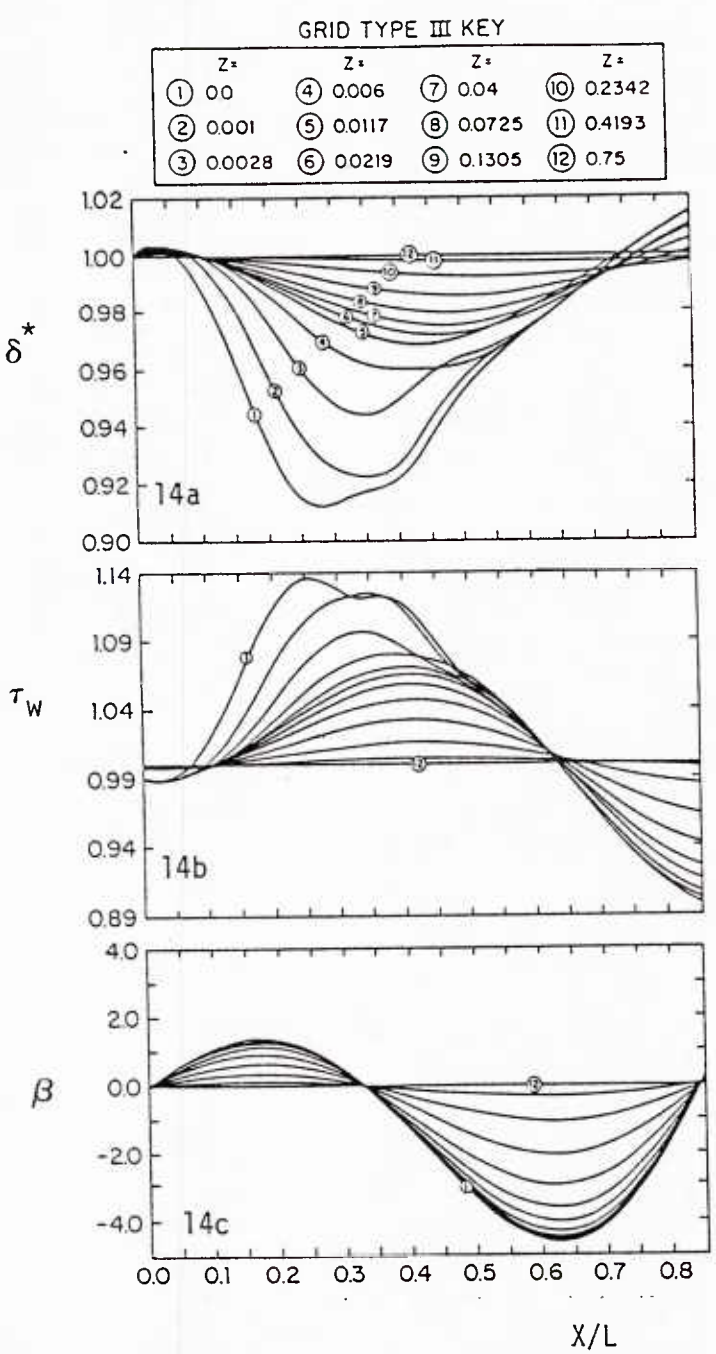

Figure 14a-c. Small-Amplitude-Wave Solution Displacement Thickness δ^* and Wall-Shear-Stress Magnitude τ_w and Angle β: Ak=.01

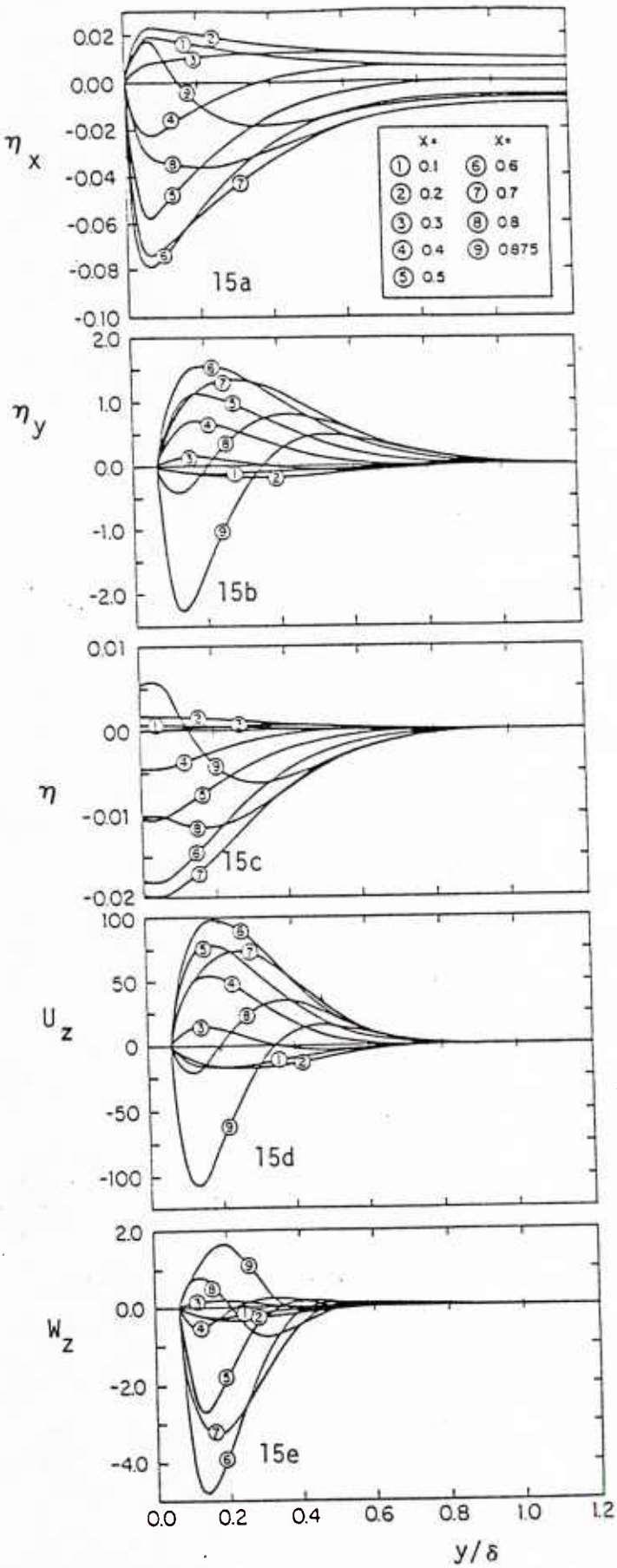

Figure 15a-c. Small-Amplitude-Wave Solution Free-Surface Behavior Within the Boundary Layer: Ak=.01

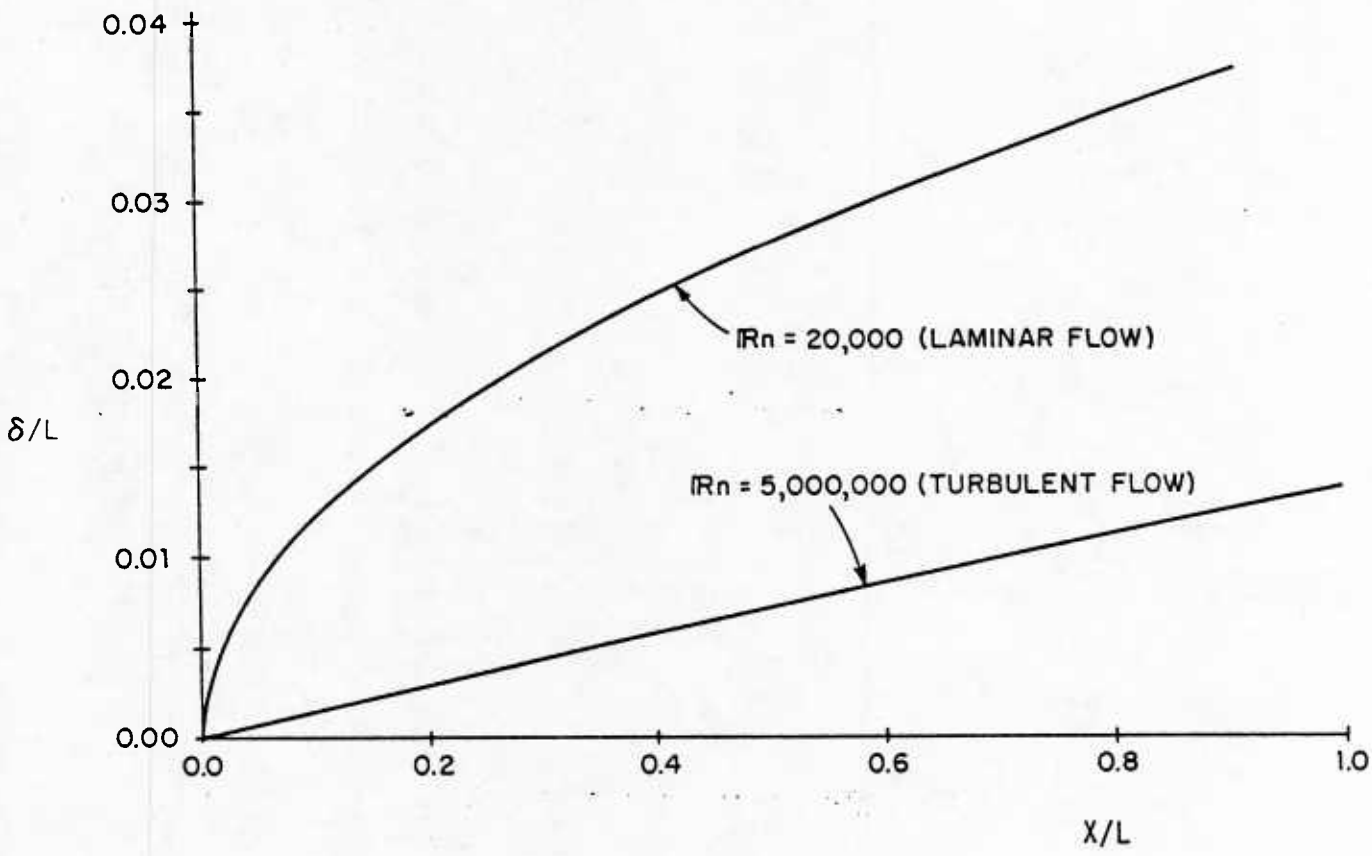

Figure 16. Boundary Layer Thickness

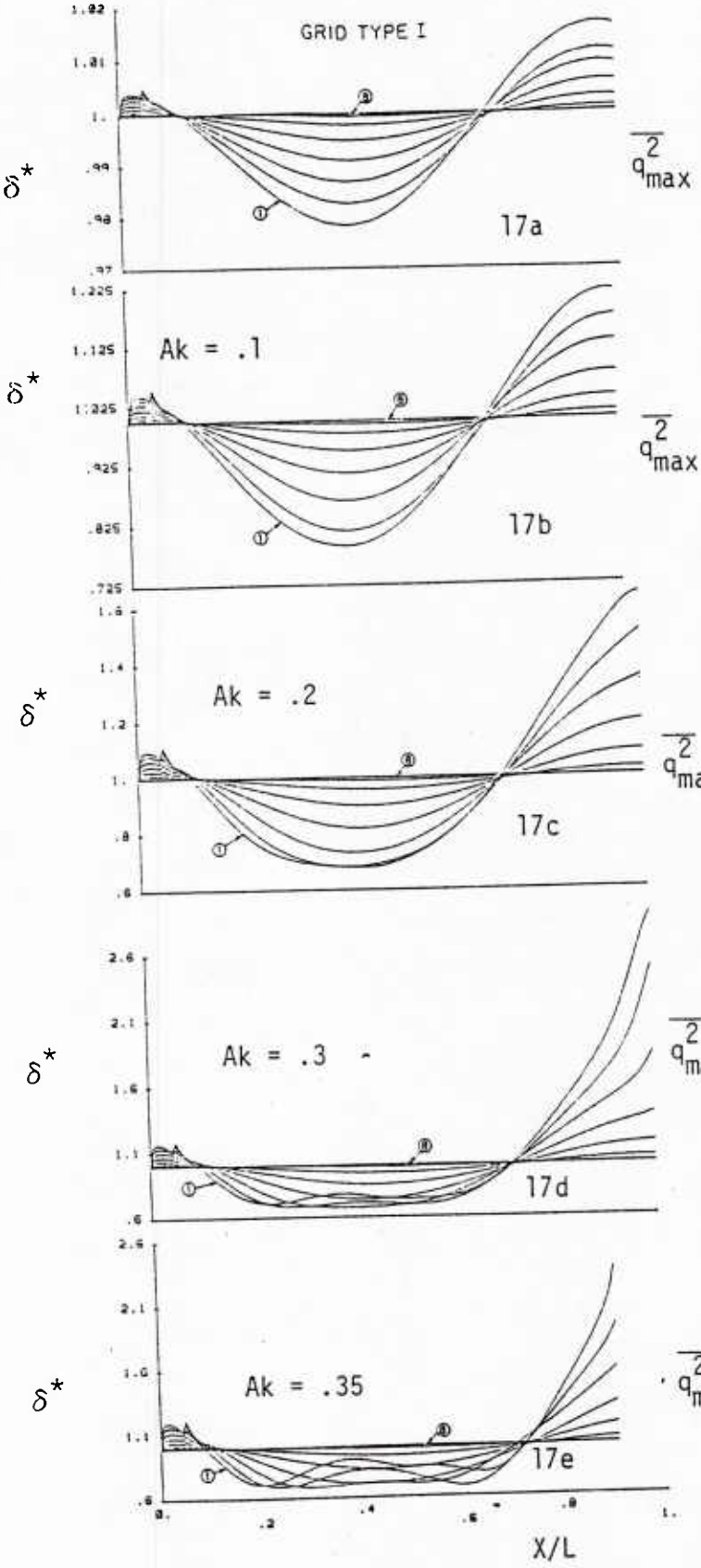

Figure 17a-e. Normalized Displacement Thickness δ^*

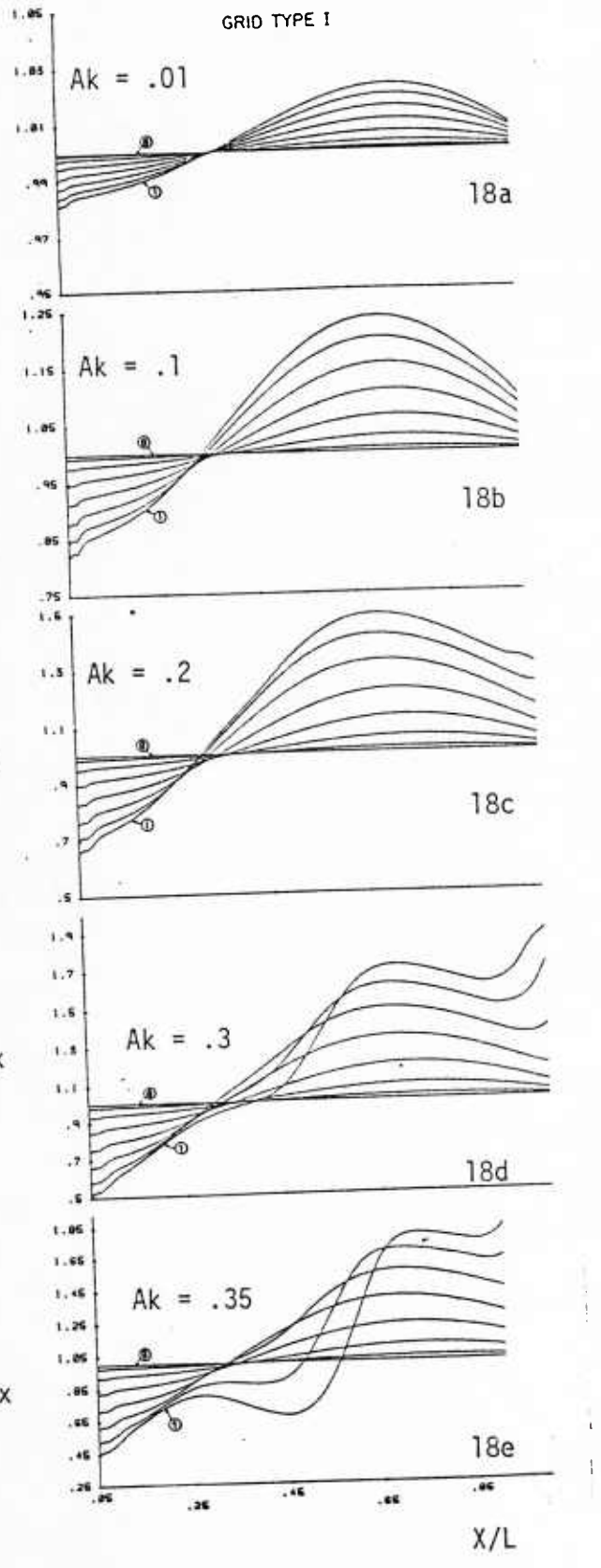

Figure 18a-e. Normalized Maximum Value of Turbulent Kinetic Energy in Outer 3/4 of δ $\overline{q^2_{max}}$

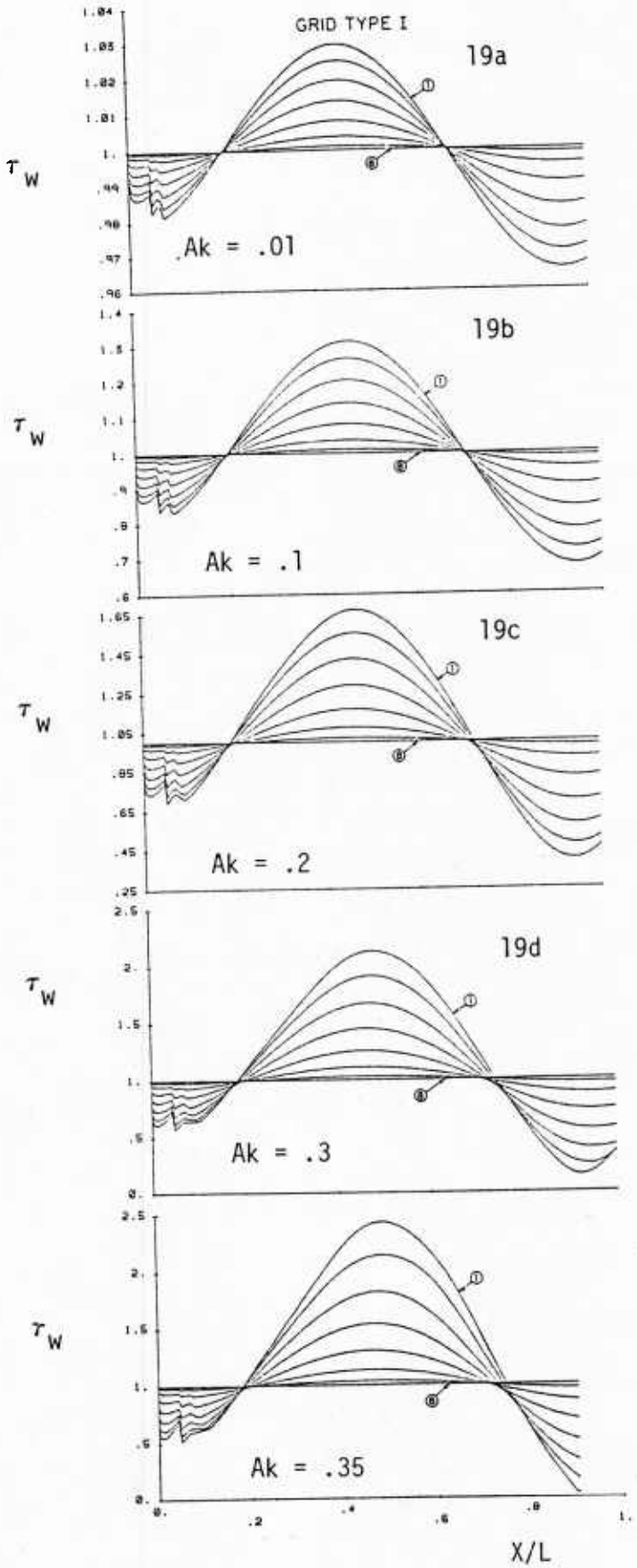

Figure 19a-e. Normalized Wall-Shear-Stress Magnitude τ_w

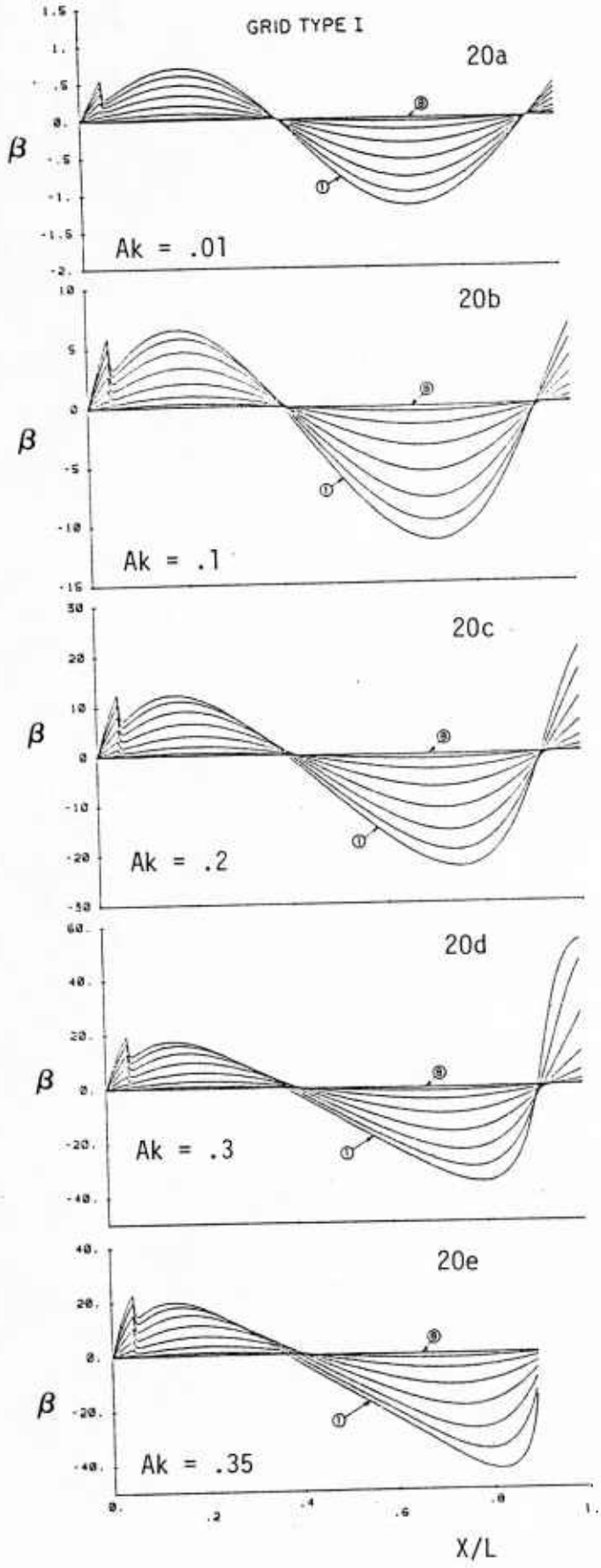

Figure 20a-e. Wall-Shear-Stress Angle β (Degrees)

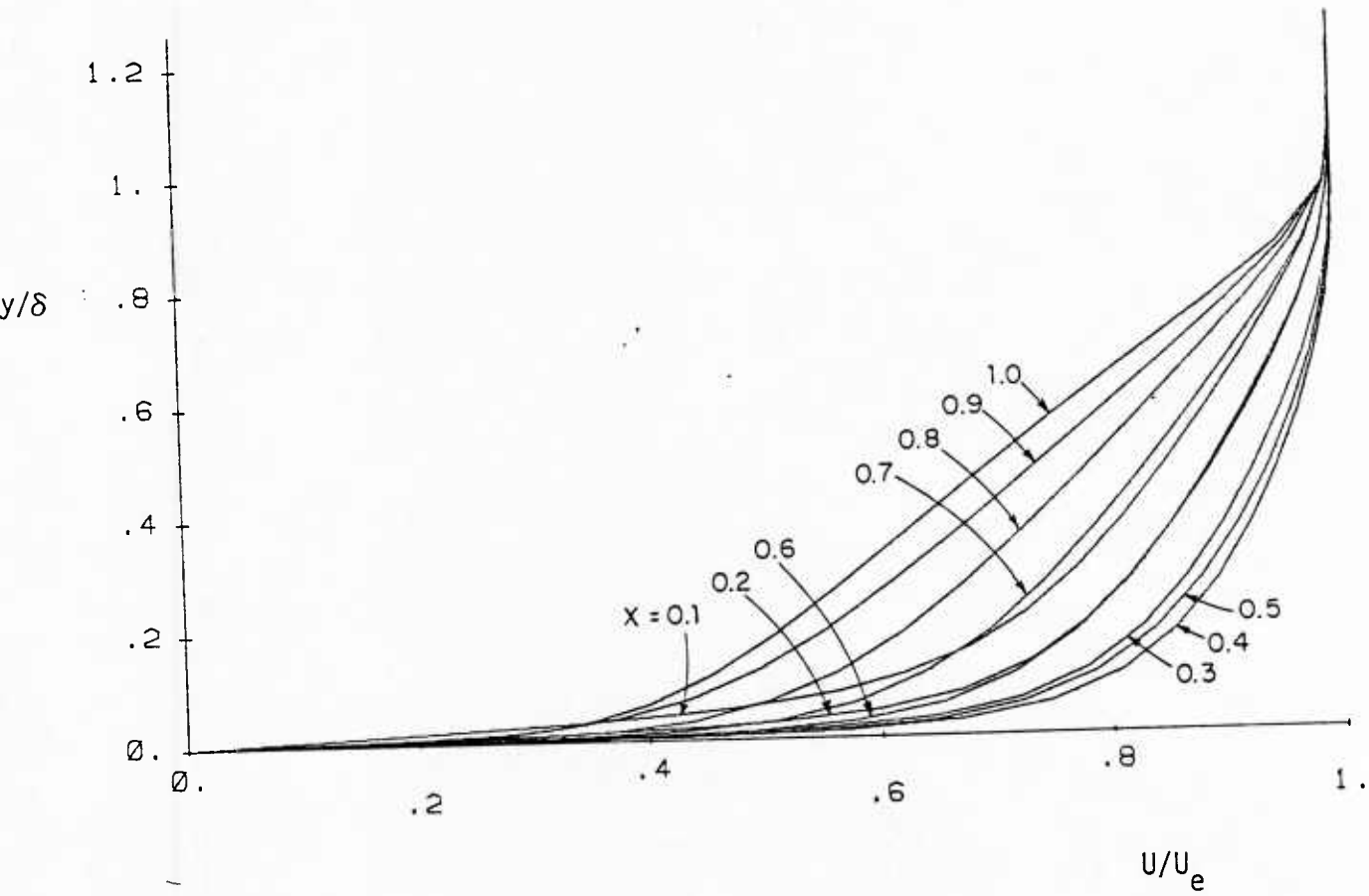

Figure 21. Streamwise Velocity Profile U/U_e Along the Mean Free Surface (z=0) at Various Cross-Planes: $_{Ak=.3}$

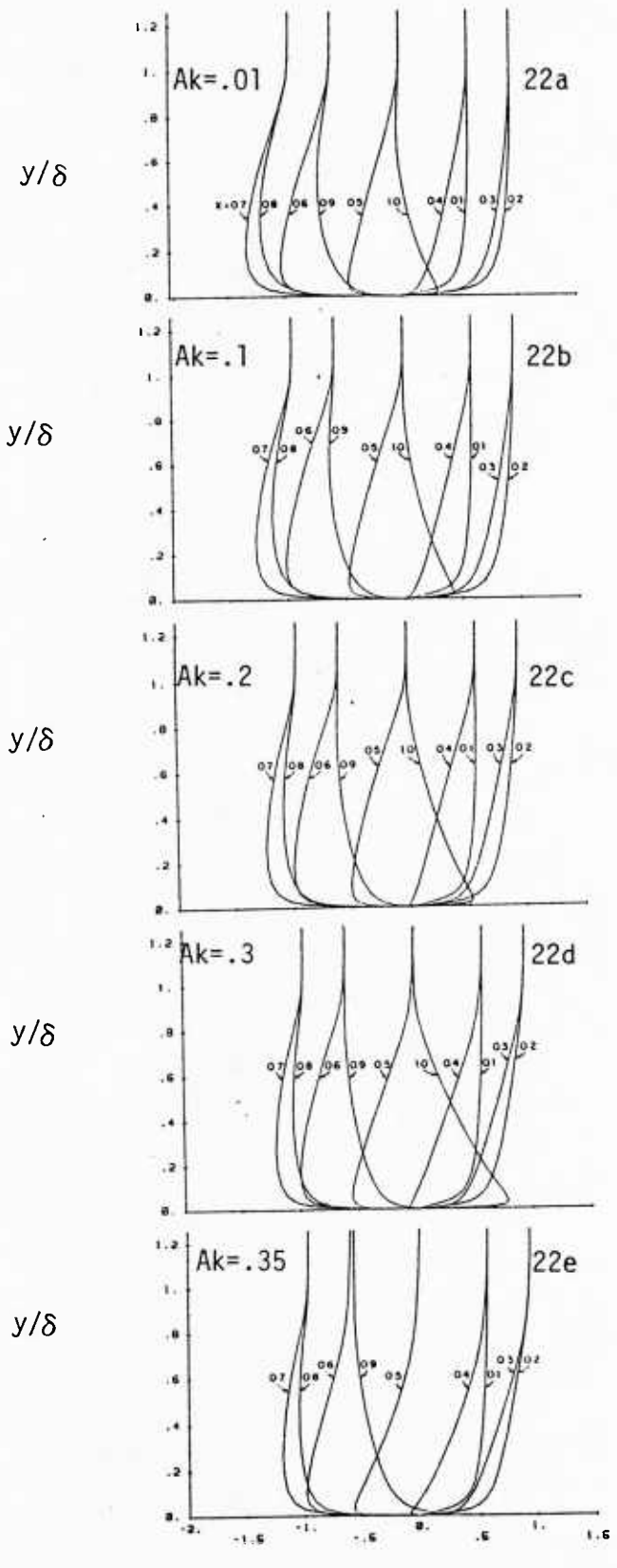

Figure 22a-e. Cross-flow Velocity Profile W/Ak Along the Mean Free Surface (z=0) at Various Cross-Planes: Ak=(.01,.1,.3,.35)

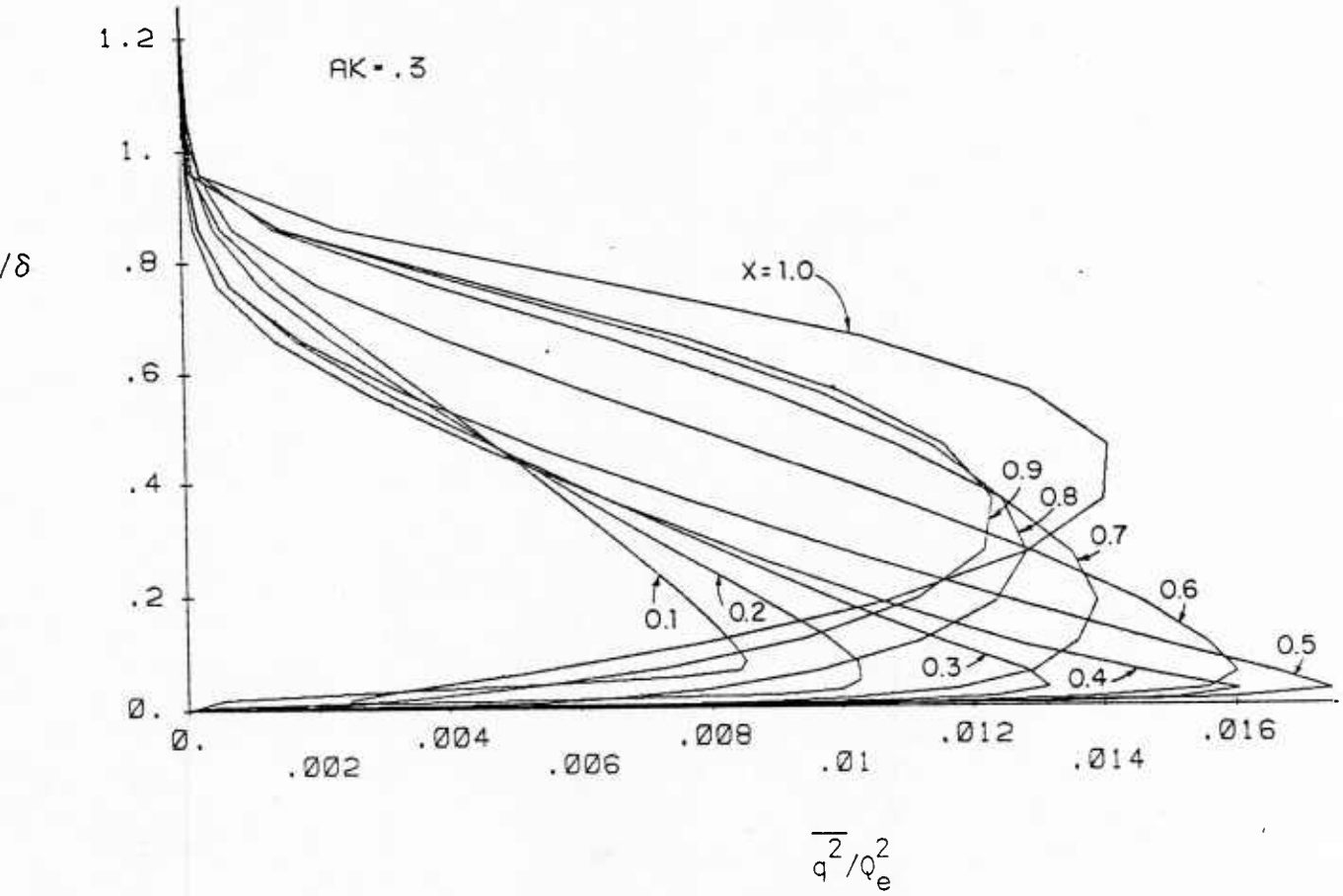

Figure 23. Turbulent Kinetic Energy Profile $\overline{q^2}/Q_e^2$ Along the Mean Free Surface (z=0) at Various Cross-Planes: Ak=.3

U.S. DISTRIBUTION LIST

Commander
David W. Taylor Naval Ship
R & D Center (ATTN: Code 1505)
Bldg. 19, Room 129B
Bethesda, Maryland 20084

Commander
Naval Sea Systems Command
Washington, D.C. 20362
ATTN: 05R22

Commander
Naval Sea Systems Command
Washington, D.C. 20362
ATTN:55W (R. Keane, Jr.)

Commander
Naval Sea Systems Command
Washington, D.C. 20362
ATTN: 55W3 (W. Sandberg)

Commander
Naval Sea Systems Command
Washington, D.C. 20362
ATTN: 50151 (C. Kennell)

Commander
Naval Sea Systems Command
Washington, D.C. 20362
ATTN: 56X12 (C.R. Crockett)

Commander
Naval Sea Systems Command
Washington, D.C. 20362
ATTN: 63R31 (T. Pierce)

Commander
Naval Sea Systems Command
Washington, D.C. 20362
ATTN: 55X42 (A. Paladino)

Commander
Naval Sea Systems Command
Washington, D.C. 20362
ATTN: 99612 (Library)

Director
Defense Documentation Center
5010 Duke Street
Alexandria, VA 22314

Library of Congress
Science & Technology Division
Washington, D.C. 20540

Naval Underwater Weapons Research
& Engineering Station (Library)
Newport, RI 02840

Office of Naval Research
800 N. Quincy Street
Arlington, VA 22217
ATTN: Dr. C.M. Lee, Code 432

Commanding Officer (L31)
Naval Civil Engineering Laboratory
Port Hueneme, CA 93043

Commander
Naval Ocean Systems Center
San Diego, CA 92152
ATTN: Library

Library
Naval Underwater Systems Center
Newport, RI 02840

Charleston Naval Shipyard
Technical Library
Naval Base
Charleston, SC 29408

Norfolk Naval Shipyard
Technical Library
Portmoth, VA 23709

Puget Sound Naval Shipyard
Engineering Library
Bremerton, WA 98314

Long Beach Naval Shipyard
Technical Library (246L)
Long Beach, CA 90801

Mare Island Naval Shipyard
Shipyard Technical Library (202.3)
Vallejo, CA 94592

Assistant Chief Design Engineer
for Naval Architecture (Code 250)
Mare Island Naval Shipyard
Vallejo, CA 94592

U.S. Naval Academy
Annapolis, MD 21402
ATTN: Technical Library

Naval Postgraduate School
Monterey, CA 93940
ATTN: Library (2124)

Study Center
National Maritime Research Center
U.S. Merchant Marine Academy
Kings Point, LI, New York 11024

The Pennsylvania State University
Applied Research Laboratory (Library)
P.O. Box 30
State College, PA 16801

Dr. B. Parkin, Director
Garfield Thomas Water Tunnel
Applied Research Laboratory
P.O. Box 30
State College, PA 16801

Bolt, Beranek & Newman (Library)
50 Moulton Street
Cambridge, MA 02138

Cambridge Acoustical Associates, Inc.
54 Rindge Ave Extension
Cambridge, MA 02140

R & D Manager
Electric Boat Division
General Dynamics Corporation
Groton, Conn 06340

Gibbs & Cox, Inc. (Tech. Info. Control)
21 West Street
New York, NY 10006

Tracor Hydronautics, Inc. (Library)
Pindell School Rd.
Laurel, MD 20810

Newport New Shipbuilding and
Dry Dock Co. (Tech. Library)
4101 Washington Ave.
Newport News, VA 23607

Society of Naval Architects and
Marine Engineers (Tech. Library)
One World Trade Center, Suite 1369
New York, NY 10048

Sperry Systems Management Division
Sperry Rand Corporation (Library)
Great Neck, NY 10020

Stanford Research Institute
Menlo Park, CA 94025
ATTN: Library

Southwest Research Institute
P.O. Drawer 28510
San Antonio, TX 78284
ATTN: Dr. H. Abramson

Mr. Robert Taggart
9411 Lee Highway, Suite P
Fairfax, VA 22031

Ocean Engr. Department
Woods Hole Oceanographic Inc.
Woods Hole, Mass 02543

Worcester Polytechnic Inst.
Alden Research Lab (Tech Library)
Worcester, MA 01609

Applied Physics Laboratory
University of Washington (Tech. Library)
1013 N. E. 40th Street
Seattle, WA 98105

University of California
Naval Architecture Department
Berkeley, CA 94720
ATTN: Profs. Webster, Paulling,
Wehausen & Library

California Institute of Technology
Pasadena, CA 91109
ATTN: Library

Engineering Research Center
Reading Room
Colorado State University
Foothills Campus
Fort Collins, CO 80521

Florida Atlantic University
Ocean Engineering Department
Boca Raton, Florida 33432
ATTN: Technical Library

Gordon McKay Library
Harvard University
Pierce Hall
Cambridge, MA 02138

Department of Ocean Engineering
University of Hawaii (Library)
2565 The Mall
Honolulu, Hawaii 96822

Institute of Hydraulic Research
The University of Iowa
Iowa City, Iowa 52242
ATTN: Library, Landweber, Patel

Prof. O. Phillips
Mechanics Department
The John Hopkins University
Baltimore, MD 21218

Kansas State University
Engineering Experiment Station
Seaton Hall
Manhattan, Kansas 66502
ATTN: Prof. D. Nesmith

University of Kansas
Chm Civil Engr Department Library
Lawrence, Kansas 60644

Fritz Engr. Laboratory Library
Department of Civil Engr
Lehigh University
Bethelehem, Pa 18015

Department of Ocean Engineering
Massachusetts Institute of Technology
Cambridge, MA 02139
ATTN: Profs. Leehey & Kerwin

Engineering Technical Reports
Room 10-500
Massachusetts Institute of Technology
Cambridge, MA 02139

St. Anthony Falls Hydraulic Laboratory
University of Minnesota
Mississippi River at 3rd Av., SE
Minneapolis, MN 55414
ATTN: Dr. Arndt & Library

Department of Naval Architecture
and Marine Engineering-North Campus
University of Michigan
Ann Arbor, Michigan 48109
ATTN: Library

Davidson Laboratory
Stevens Institute of Technology
711 Hudson Street
Hoboken, NJ 07030
ATTN: Library

Applied Research Laboratory
University of Texas
P.O. Box 8029
Austin, TX 78712

Stanford University
Stanford, CA 94305
ATTN: Engineering Library, Dr. Street

Webb Institute of Naval Architecture
Crescent Beach Road
Glen Cove, LI, NY 11542
ATTN: Library

National Science Foundation
Engineering Divison Library
1800 G Street NW
Washington, DC 20550

Mr. John L. Hess
4338 Vista Street
Long Beach, CA 90803

Dr. Tuncer Cebeci
Mechanical Engineering Dept.
California State University
Long Beach, CA 90840

Science Applications, Inc.
134 Holiday Court, Suite 318
Annapolis, MD 21401